

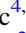





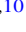



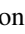

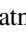





Seven Years of Coordinated Chandra–NuSTAR Observations of SN 2014C Unfold the Extreme Mass-loss History of Its Stellar Progenitor

Daniel Brethauer^{1,2} , Raffaella Margutti^{1,3} , Dan Milisavljevic^{4,5} , Michael F. Bietenholz⁶ , Ryan Chornock¹ ,
Deanne L. Coppejans⁷ , Fabio De Colle⁸ , Aprajita Hajela² , Giacomo Terreran^{9,10} , Felipe Vargas⁸ ,
Lindsay DeMarchi² , Chelsea Harris¹¹ , Wynn V. Jacobson-Galán¹ , Atish Kamble¹² , Daniel Patnaude¹² , and
Michael C. Stroh² 

¹ Department of Astronomy, University of California, Berkeley, CA 94720-3411, USA; daniel_brethauer@berkeley.edu

² Center for Interdisciplinary Exploration and Research in Astrophysics (CIERA) and Department of Physics and Astronomy, Northwestern University, Evanston, IL 60208, USA

³ Department of Physics, University of California, 366 Physics North MC 7300, Berkeley, CA 94720, USA

⁴ Purdue University, Department of Physics and Astronomy, 525 Northwestern Avenue, West Lafayette, IN 47907, USA

⁵ Integrative Data Science Initiative, Purdue University, West Lafayette, IN 47907, USA

⁶ Department of Physics and Astronomy, York University, 4700 Keele Street, Toronto, M3J 1P3, Ontario, Canada

⁷ Department of Physics, University of Warwick, Coventry CV4 7AL, UK

⁸ Instituto de Ciencias Nucleares, Universidad Nacional Autónoma de México, A.P. 70-543 04510, Mexico City, Mexico

⁹ Las Cumbres Observatory, 6740 Cortona Drive, Suite 102, Goleta, CA 93117-5575, USA

¹⁰ Department of Physics, University of California, Santa Barbara, CA 93106-9530, USA

¹¹ Department of Physics and Astronomy, Michigan State University, East Lansing, MI 48824, USA

¹² Center for Astrophysics—Harvard & Smithsonian, 60 Garden Street, Cambridge, MA 02138, USA

Received 2022 June 8; revised 2022 August 17; accepted 2022 August 17; published 2022 November 10

Abstract

We present the results from our 7 yr long broadband X-ray observing campaign of SN 2014C with Chandra and NuSTAR. These coordinated observations represent the first look at the evolution of a young extragalactic SN in the 0.3–80 keV energy range in the years after core collapse. We find that the spectroscopic metamorphosis of SN 2014C from an ordinary type Ib SN into an interacting SN with copious hydrogen emission is accompanied by luminous X-rays reaching $L_x \approx 5.6 \times 10^{40} \text{ erg s}^{-1}$ (0.3–100 keV) at ~ 1000 days post-explosion and declining as $L_x \propto t^{-1}$ afterwards. The broadband X-ray spectrum is of thermal origin and shows clear evidence for cooling after peak, with $T(t) \approx 20 \text{ keV}(t/t_{\text{pk}})^{-0.5}$. Soft X-rays of sub-keV energy suffer from large photoelectric absorption originating from the local SN environment with $\text{NH}_{\text{int}}(t) \approx 3 \times 10^{22}(t/400 \text{ days})^{-1.4} \text{ cm}^{-2}$. We interpret these findings as the result of the interaction of the SN shock with a dense ($n \approx 10^5 - 10^6 \text{ cm}^{-3}$), H-rich disk-like circumstellar medium (CSM) with inner radius $\sim 2 \times 10^{16} \text{ cm}$ and extending to $\sim 10^{17} \text{ cm}$. Based on the declining $\text{NH}_{\text{int}}(t)$ and X-ray luminosity evolution, we infer a CSM mass of $\sim (1.2f - 2.0\sqrt{f})M_{\odot}$, where f is the volume filling factor. We place SN 2014C in the context of 121 core-collapse SNe with evidence for strong shock interaction with a thick circumstellar medium. Finally, we highlight the challenges that the current mass-loss theories (including wave-driven mass loss, binary interaction, and line-driven winds) face when interpreting the wide dynamic ranges of CSM parameters inferred from observations.

Unified Astronomy Thesaurus concepts: [Core-collapse supernovae \(304\)](#); [X-ray astronomy \(1810\)](#); [Shocks \(2086\)](#); [Circumstellar shells \(242\)](#)

Supporting material: machine-readable table

1. Introduction

Observational studies of evolved massive stars are starting to reveal an eventful history of mass loss as these stars approach core collapse. Observational evidence has been accumulating from a variety of independent lines, including: the direct detection of pre-supernova outbursts from across the mass spectrum of exploding stars (e.g., Pastorello et al. 2007, 2013; Margutti et al. 2014; Ofek et al. 2014; Pastorello et al. 2018; Strotjohann et al. 2021; Jacobson-Galán et al. 2022b); bright UV emission in type IIP supernovae (SNe IIP) at early times (e.g., Morozova et al. 2018; Bostroem et al. 2019; Morozova et al. 2020; Dessart & John Hillier 2022); narrow spectral lines originating from a dense circumstellar medium ionized by the

explosion’s shock (as in type IIn, type Ibn, and type Icn SNe; e.g., Schlegel 1990; Filippenko 1997; Pastorello et al. 2008; Perley et al. 2022); re-brightening of optical light curves (e.g., Sollerman et al. 2020; Jin et al. 2021; Soraisam et al. 2022); and luminous X-ray and radio emission powered by efficient conversion of shock kinetic energy into radiation as the SN shock is decelerated in the environment by mass lost by the star before stellar demise (e.g., Chevalier & Fransson 2006; Soderberg et al. 2006; Dwarkadas et al. 2010; Chevalier & Fransson 2017; Stroh et al. 2021). Here we present the results from a coordinated campaign on SN 2014C with the Chandra X-ray Observatory (CXO) and the Nuclear Spectroscopic Telescope Array (NuSTAR) during the first 7 yr after core collapse, and update the analysis by Margutti et al. (2017). These observations map the evolution of the emission from the interaction of an H-stripped SN shock with an H-rich medium in the soft and hard X-rays for the first time.

SN 2014C originally attracted the attention of the SN community because of its highly unusual spectroscopic metamorphosis

from an ordinary H-stripped core-collapse SN type Ib into an SN with clear signs of interaction with an H-rich medium, as documented in Milisavljevic et al. (2015; see Mauerhan et al. 2018 for a follow-up study). The optical spectroscopic metamorphosis was accompanied by rising luminous radio and X-ray emission (Anderson et al. 2016; Margutti et al. 2017; Brethauer et al. 2020; Bietenholz et al. 2021a, 2021b; Thomas et al. 2022), as well as luminous infrared emission (Tinyanont et al. 2016, 2019). Despite different modeling assumptions in those papers, and in theoretical investigations such as Harris & Nugent (2020) and Vargas et al. (2022), a concordant picture emerged that associates the SN 2014C phenomenology with the presence of dense H-rich circumstellar material (CSM) in the immediate vicinity of an H-poor SN. Furthermore, the analysis of archival pre-explosion images pointed at a low-mass star of $M_{\text{ZAMS}} \approx 11 M_{\odot}$ as progenitor (Milisavljevic et al. 2015; Sun et al. 2020).

Clear signs of H-rich CSM interaction have occurred in other stripped envelope explosion types; SNe 2001em (Chugai & Chevalier 2006), 2004dk (Mauerhan et al. 2018), 2017dio (Kuncarayakti et al. 2018), and 2019yvr (Kilpatrick et al. 2021), as well as superluminous SNe iPTF13ehe, iPTF15esb, iPTF16bad (Yan et al. 2017), and 2017ens (Andrews et al. 2019) all showed a delayed appearance of $H\alpha$ emission. Similarly, late-time radio emission that is believed to be connected to this phenomenology has been observed in SNe 2001em (Schinzel et al. 2009), 2003gk (Bietenholz et al. 2014), 2004C (DeMarchi et al. 2022), 2007bg (Salas et al. 2013), PTF11qcj (Corsi et al. 2014), VT J121001+495647 (Dong et al. 2021), and others identified in Stroh et al. (2021).

Several explanations have been proposed to explain these observations, ranging from luminous blue variable (LBV)–like eruptions (e.g., Smith & Owocki 2006; Smith 2014), to stellar H-envelope ejection as a result of binary interaction (e.g., Podsiadlowski et al. 1992), to internal gravity-wave-driven mass ejections proposed in Quataert & Shiode (2012), to nuclear burning instabilities (Smith & Arnett 2014). By assembling a large sample of 121 core-collapse SNe with signatures of interaction with a thick CSM, we show how each of these mechanisms might naturally explain only a portion of the mass-loss parameter space of evolved massive stars.

The paper is organized as follows. In Section 2, we present the analysis of our broadband X-ray campaign of SN 2014C with the CXO and NuSTAR. In Section 3 we model these observations and derive our inferences on the SN shock and circumstellar environment. We discuss our findings within the broader context of a large sample of 121 core-collapse SNe (see Table 1) with observational signatures of interaction with a dense medium in Section 4. Finally, we discuss different mass-loss scenarios, including line-driven winds (Section 4.2.1), interaction with a stellar companion (Section 4.2.2), and internal gravity-wave-driven mass loss (Section 4.2.3). Conclusions are drawn in Section 5. In Appendix A we provide a detailed accounting of each individual interacting SN in our sample, including classification, modeled properties from other literature, and our methods for filling in information that was not explicitly provided.

Following Freedman et al. (2001), we adopt a distance of 14.7 ± 0.6 Mpc for the host galaxy of SN 2014C (NGC 7331). Times are referred to the time of first light from Margutti et al. (2017), which is 2013 December 30 ± 1 day (corresponding to MJD 56656 ± 1). Uncertainties are quoted at 1σ confidence level and upper limits at the 3σ confidence level unless stated otherwise.

2. Soft and Hard X-Ray Observations

We present a homogeneous analysis of our entire broadband X-ray campaign of SN 2014C for the first ~ 2307 days of the evolution, using the CXO and NuSTAR. For consistency, we also reanalyze the X-ray data acquired at $\delta t < 500$ days, which we originally published in Margutti et al. (2017). While the present paper was in an advanced stage of preparation, the paper by Thomas et al. (2022) appeared on the arXiv presenting the data from our extensive soft and hard-X-ray campaign of SN 2014C. We comment as appropriate in the remainder of the paper on differences between our analysis and the independent one of Thomas et al. (2022). A key difference between the two analyses is that our approach accounts for background contamination at higher energies and therefore produces a more accurate model. This data set offers the unprecedented opportunity to study the evolution of the hard X-ray emission from an extragalactic SN over a baseline of 7 yr.

2.1. Soft X-Ray Observations with the CXO

Prior to the explosion, the field of SN 2014C was observed by the CXO on 2001 January 27 (PI Zezas, ID 2198) for a total exposure time of ~ 29.5 ks. No X-ray emission was detected at the location of SN 2014C with a 3σ absorbed flux limit of $< 2.8 \times 10^{-15}$ erg s $^{-1}$ cm $^{-2}$ (0.3–10 keV). We refer the reader to Margutti et al. (2017) for more details on CXO pre-explosion observations.

We started monitoring SN 2014C with the CXO on 2014 November 3 ($\delta t = 308$ days since explosion, PI Soderberg, ID 16005). Further CXO observations were acquired starting from 2015 January 30 to 2020 April 18, ≈ 1 to ≈ 6 yr post-explosion, with a total exposure time of ~ 242 ks (Table 2, PI Margutti).

We reduced the CXO data with the software package CIAO v. 4.12 by applying standard ACIS filtering criteria and using the latest calibration database (CALDB v. 20190813). We used the `wavdetect` task within CIAO to perform blind point-source detection. A bright X-ray source is blindly detected with high confidence ($> 40\sigma$) at the location of SN 2014C throughout these observations. The corresponding significance of detection and count-rates are reported in Appendix B, Table 2. We note that the observed 0.5–8 keV count-rate increases until $\delta t \approx 1258$ days as a result of the combination of the larger intrinsic luminosity of the source and the smaller intrinsic absorption with time.

For each observation, we extracted a spectrum from a $1''.5$ radius region around the source using `specextract` within CIAO. We extracted the background spectrum from a large source-free region away from chip edges of $\sim 20''$. We fit the spectrum from each CXO observation independently with the exception of IDs 18343+21077 and 21640+23216. Each pair of observation IDs were acquired very close in time ($\Delta t/t < 10^{-3}$) and can be thus considered effectively part of the same epoch of observations. For this first round of spectral modeling, we used an absorbed power-law model `tbabs * ztbabs * pow` in XSPEC. We adopted a Galactic neutral hydrogen column density in the direction of SN 2014C as $N_{\text{H,MW}} = 6.14 \times 10^{20}$ cm $^{-2}$ (Kalberla et al. 2005). We employed Cash statistics to constrain the spectral parameters and their uncertainties. The inferred best-fitting parameters as well as absorbed and unabsorbed fluxes are reported in Appendix B, Table 3. Our measurements are consistent with the X-ray analysis presented in Jin & Kong (2019).

2.2. Hard X-Ray Observations with NuSTAR

We acquired hard X-ray (3–79 keV) observations of SN 2014C with NuSTAR starting on 2015 January 29 ($\delta t \sim 400$ days) through 2020 April 30 ($\delta t \sim 2300$ days, PI Margutti), for a total exposure of ~ 347 ks. Since the emission from the background largely dominates the spectrum above ~ 40 keV, in the following, we focus our analysis on the 3–40 keV spectral window. We extracted and cleaned the event files with `nupipeline` and `nuproducts` within NuSTAR-DAS (v.1.9.5) using standard filtering criteria and the latest files available in the NuSTAR calibration database (CALDB v.20190607). Specifically, for the data screening and filtering step, we follow the updated prescriptions of NuSTAR-DAS (v.1.9.5).

With these parameters, we find that a source of hard X-ray emission is blindly detected at the location of SN 2014C with high significance ($>15\sigma$ confidence level, see Appendix B, Table 4) throughout the entire duration of our monitoring campaign. Importantly, these observations establish SN 2014C as the first SN with well-monitored bright hard X-ray emission over its first ~ 7 yr of evolution post-explosion.

For each observation, we extracted a source spectrum from a region of $1'$ radius around the position of SN 2014C. For the background spectrum, we used a source-free annulus region centered at the source location with an inner and outer radius of $1'$ and $3'$, respectively. NuSTAR observations complement the CXO observations at higher X-ray energies. In Section 2.3 we exploit the high angular resolution of coordinated CXO observations to model and account for the partial contamination of the low-energy NuSTAR data by unrelated sources in the host galaxy of SN 2014C, which results from the larger NuSTAR point-spread function (PSF), with an FWHM of $\sim 18''$.

2.3. Joint Spectral Analysis of CXO and NuSTAR Data

In this section we perform broadband X-ray spectral modeling in the 0.3–40 keV energy range using observations from both CXO and NuSTAR.

We performed a joint spectral fit of each of the epochs for which we have coordinated CXO and NuSTAR observations (Appendix B, Table 5). Following Margutti et al. (2017), we use an absorbed thermal bremsstrahlung spectral model (`tbabs*ztbabs*bremss`) for the SN emission.¹³ While the fine angular resolution of the CXO allows for the CXO spectrum to be entirely dominated by the SN emission, the more extended NuSTAR PSF includes important contributions from the host-galaxy emission that is unrelated to the SN. We account for the presence of contamination in the NuSTAR spectrum by adding an absorbed power-law (`tbabs*pow`) spectral component to model the NuSTAR data.

We initially tie the `bremss` model parameters of CXO and NuSTAR observations and fit for the intrinsic neutral hydrogen column density ($N_{\text{H,int}}$), plasma temperature (T), and the emission measure (EM) associated with the `bremss` model and the photon index (Γ) of the power-law component. The best-fitting power-law model obtained in this way quantifies the contribution of the contamination by the host-galaxy emission

to the NuSTAR spectrum. We then freeze the power-law model parameters to the best-fitting values obtained in the previous step, untie the hard and soft X-ray EMs and perform a final joint-fit to constrain the spectral parameters associated with the bremsstrahlung emission. Even with the bremsstrahlung normalization constants untied between CXO and NuSTAR, they were consistently well within 10% of each other. In this way we account for potential CXO-NuSTAR intercalibration uncertainties.

Table 5 in Appendix B reports the inferred best-fitting parameters values and the derived absorbed and unabsorbed fluxes in the 0.3–100 keV range, plasma temperature, and intrinsic neutral hydrogen column density from the broadband X-ray spectral fitting. The best-fitting spectra of SN 2014C are portrayed in Figures 1 and 2. The evolution of the $N_{\text{H,int}}$, the plasma temperature T and the 0.3–100 keV X-ray luminosity are shown in Figures 3, 4, and 5, respectively. Our findings in the first 500 days of evolution are consistent with the results presented by Margutti et al. (2017), and broadly similar to Thomas et al. (2022). However, Thomas et al. (2022) did not account for the contamination of the NuSTAR PSF by unrelated sources. We find that this leads to a systematic underestimate of the plasma temperature T . We can reproduce the $T \approx 10$ keV values reported by Thomas et al. (2022) by setting to zero the normalization of the power-law spectral component that quantifies the contamination by other X-ray sources and by including the NuSTAR data above 50 keV in the fit, which are background dominated.

From our analysis, we find that $N_{\text{H,int}}(t)$ shows a monotonic decline with $N_{\text{H,int}}(t) \propto t^{-1.4}$ from $\sim 2.7 \times 10^{22} \text{ cm}^{-2}$ at $\delta t \sim 396$ days to $\sim 3 \times 10^{21} \text{ cm}^{-2}$ at $\delta t \sim 2307$ days, which suggests that the $N_{\text{H,int}}$ is completely dominated by material outside of the Milky Way and local to the SN explosions at all times (Figure 3). The temperature peaks at $T \sim 23$ keV at $\delta t \approx 500$ –600 days, to later decay as $\propto t^{-0.5}$ until the end of our monitoring at $\delta t \approx 2300$ days, indicating a deviation from adiabatic expansion ($T(t) \propto t^{-2}$ (Figure 4)). The resulting 0.3–100 keV luminosity inferred from the unabsorbed fluxes reaches $L_x \sim 5.5 \times 10^{40} \text{ erg s}^{-1}$ at ~ 1000 days. The post-peak decline is currently well described by a $\propto t^{-1}$ decay (Figure 5). The physical implications of these observational findings are discussed in detail in the following section.

Finally, we note the presence of an excess of emission with respect to the thermal bremsstrahlung model in the energy interval ~ 6.5 –7.1 keV in our broadband X-ray modeling (Figures 1, 2 and 6). We fit the emission in the energy range 5–9 keV with a Gaussian model in addition to the inferred best-fit bremsstrahlung and power-law models. As noted in Margutti et al. (2017), we associate this emission with H- and He-like Fe atom transitions, in particular with the resulting $K\alpha$ emission line. Table 6 reports the best-fitting values and the inferred unabsorbed flux in the 6.5–7.1 keV energy range of the Gaussian component. Unfortunately, the data lack the spectral resolution and signal-to-noise ratio to further constrain the potentially complex line emission from highly ionized iron that might be expected (Mewe et al. 1985, 1986; Liedahl et al. 1995).

3. Inferences on the Shock and Environment Properties

In this section we derive inferences on the shock and environment physical parameters using the constraints on the temperature $T(t)$, intrinsic neutral hydrogen absorption $N_{\text{H,int}}(t)$,

¹³ Note that the Fe line emission and the underlying continuum do not necessarily originate from the same emitting region, and we thus avoid using the `vapec` model of collisionally ionized diffuse gas adopted by Thomas et al. (2022).

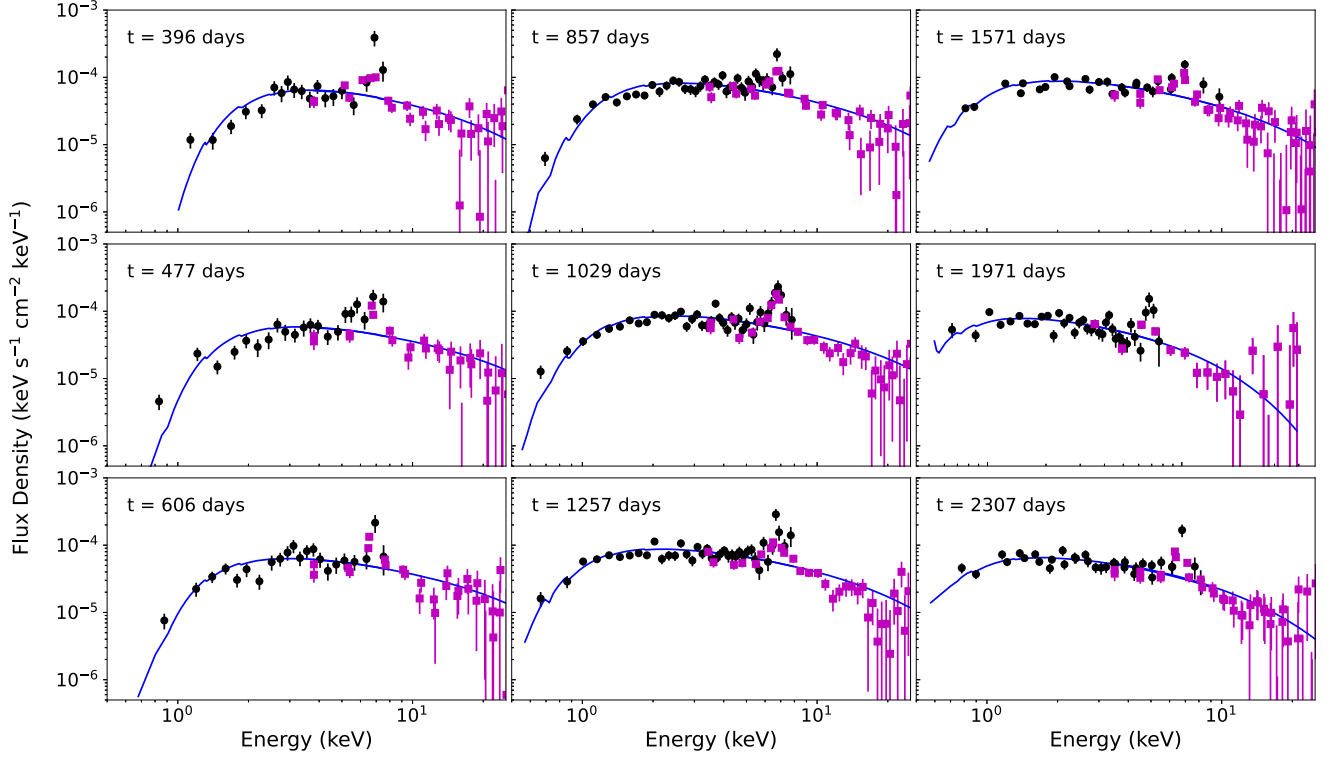


Figure 1. Broadband (0.5–40 keV) X-ray spectrum of SN 2014C acquired with coordinated CXO (black filled circles) and NuSTAR (magenta squares) observations spanning from $\delta t = 396$ to 2307 days since explosion. In each panel, a thick blue line marks the best-fitting absorbed bremsstrahlung model with best-fitting spectral parameters reported in Appendix B, Table 5, and shown in Figures 3 and 4. There is an excess of emission with respect to this model (Figures 1 and 2), which, following Margutti et al. (2017), we associate the excess of emission around 6.7 keV to a $K\alpha$ line transition in highly ionized Fe atoms with one or two electrons remaining. The best-fitting parameters of the Gaussian excess are reported in Appendix B, Table 6, and the observed flux evolution of the Fe emission is shown in Figure 6.

and $EM(t)$:¹⁴

$$EM \equiv \int n_I n_e dV \approx n_I n_e V_{FS} = \frac{\rho_{FS}^2}{\mu_e \mu_I m_p^2} V_{FS} \quad (2)$$

where n_I and n_e (assumed constant over the emitting volume) are the ion and electron number densities in the shocked region, respectively, and the integral is over the emitting volume V_{FS} (i.e., the shocked region). Following Margutti et al. (2017), we identify the emitting region with the shocked CSM, i.e., the region that has been shocked by the forward shock, based on the similar velocity inferred from the $H\alpha$ line and the one inferred from the X-ray modeling. We do not repeat here the argument, and we refer the reader to Margutti et al. (2017) for details. ρ_{FS} is the shocked CSM matter density, while μ_e and μ_I are the electron mean molecular weight and the ion mean molecular weight, respectively, and they reflect the chemical composition and ionization state of the CSM. For the solar-like composition and full ionization that we assume for the CSM, $\mu_e \approx 1.25$ and $\mu_I \approx 1.15$.

¹⁴ Within *XSPEC*, the normalization of the bremsstrahlung spectrum C is defined as:

$$C = \frac{3.02 \times 10^{-15}}{4\pi \left(\frac{d_L}{\text{cm}}\right)^2} \int \frac{n_i}{\text{cm}^{-3}} \frac{n_e}{\text{cm}^{-3}} \frac{dV}{\text{cm}^{-3}} \quad (1)$$

where d_L is the luminosity distance, and the integral is the EM.

3.1. General Considerations

We start with three considerations. First, the temporal decay of the temperature of emission at $\delta t \gtrsim 500$ days (Figure 4) is a likely indication that the shock front has broken out from the densest part of the shell and is moving through additional, albeit much less dense, material. From Fransson et al. (1996), while the shock is strongly interacting with the surrounding medium, the post-shock temperature is related to the velocity of the shockwave v by the equation

$$T \approx 2.27 \times 10^9 \mu v_4^2 \text{ K} \quad (3)$$

where T is the temperature of the shocked region, μ is the mean molecular weight of the shocked medium ($1/\mu \equiv 1/\mu_e + 1/\mu_I$), and $v_4 \equiv v/(10^4 \text{ km s}^{-1})$ is the shock velocity. At peak we measure $T \approx 23 \text{ keV}$ (Figure 4), which implies $v \approx 4400 \text{ km s}^{-1}$ for a CSM with completely ionized, solar-like composition (i.e., $\mu_{FS} = 0.61$).

Second, further supporting evidence for the shockwave emerging from a dense shell is the decrease in NH_{int} with time (Figure 3). NH_{int} traces the amount of *neutral* material between the emitting region and the observer, therefore providing a lower limit on the total amount of material as we expect a fraction of the material to be ionized and hence transparent to X-rays. NH_{int} has two main components: a local contribution from the immediate environment of SN 2014C (i.e., the dense shell), and a component from material along the line of sight in the SN host galaxy, NGC 7331. The rapid and dramatic decline of $NH_{\text{int}}(t)$ indicates that it is dominated by material local to SN 2014C (i.e., the unrelated host-galaxy component is

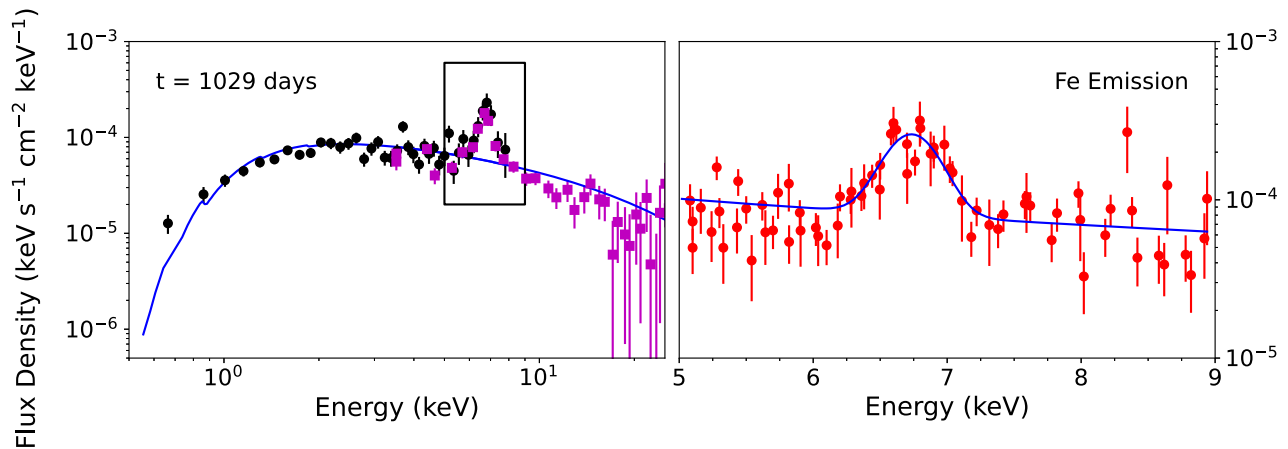


Figure 2. Broadband X-ray spectral evolution of SN 2014C as captured by CXO and NuSTAR observations at $\delta t = 1029$ days (left panel) to emphasize the Gaussian excess of emission centered around 6.7 keV within the empty black box (right panel), which, following Margutti et al. (2017), we associate to a $K\alpha$ line transition in highly ionized Fe atoms with one or two electrons remaining. Data have been rebinned to show detail. This figure follows the same color scheme as in Figure 1.

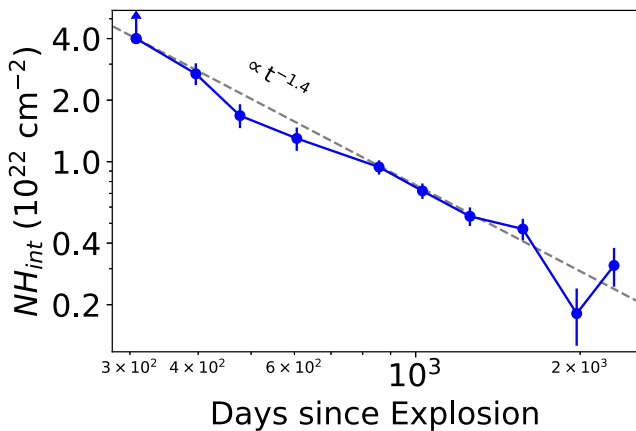


Figure 3. Evolution of intrinsic neutral hydrogen column density with time as revealed by our broadband CXO+NuSTAR spectral modeling. The first epoch lacks NuSTAR coverage, which leads to a lower limit on the $NH_{int} \gtrsim 4 \times 10^{22} \text{ cm}^{-2}$ (Margutti et al. 2017). A gray dashed line marks a $t^{-1.4}$ evolution to guide the eye.

subdominant). Importantly, the decrease in $NH_{int}(t)$ is indicative that there is progressively less material in front of the shockwave, which can be interpreted as evidence that the shockwave is moving through the CSM shell.

Third, the post-peak broadband X-ray luminosity evolution suggests a decline less steep than the $\propto t^{-2}$ that is expected in the case of purely adiabatic expansion (e.g., Margalit et al. 2022). These inferences are consistent with the shockwave moving through lower-density material after breaking out of the thick CSM shell. An intriguing possibility is that the shock at $\delta t > 1000$ days is interacting with mass lost via winds that belonged to the progenitor’s evolutionary phase that preceded the shell ejection. Alternatively, we are sampling the CSM structure developed from the interaction of winds by the stellar progenitor in two different evolutionary phases. Both options will be further discussed in Section 4.

Finally, the presence of strong and persistent iron lines in the spectra (excess over thermal bremsstrahlung shown in blue of Figure 1 and in the empty black box of Figure 2) indicates that the environment is likely to be clumpy, as was inferred for other strongly interacting SNe, e.g., SNe 1996cr (Dwarkadas et al. 2010; Dewey et al. 2011), 2006jd (Chandra et al. 2012),

and 2009ip (Margutti et al. 2014). The luminosity of iron emission can be a result of either a metallicity of $\sim 5 Z_{\odot}$ or a clumpy medium (Milisavljevic et al. 2015; Margutti et al. 2017), since the shock is more efficiently decelerated within the higher-density clumps, which leads to a lower emission T (e.g., Equation (2)) that allows more prominent iron lines, as seen in SN 1993J (Fransson et al. 1996). Based on their numerical modeling of the broadband spectra of SN 2014C, Vargas et al. (2022) found that in order to generate the observed overall continuum of absorbed thermal bremsstrahlung, their model requires a metallicity of approximately $\sim 0.5 Z_{\odot}$, further supporting the idea of a clumpy medium.

3.2. Constraints on the Shock Dynamics and Geometry of the Emitting Regions

The forward shock (FS) radius $R(t)$ evolution is constrained by both Equation (3) (from X-ray data) and by very long baseline interferometry (VLBI) radio observations (Bietenholz et al. 2021b), which provides a direct measurement of the size of the radio-emitting region. The two inferences are expected to agree with each other *if* the X-ray and radio-emitting region are the same. From Bietenholz et al. (2021b), the best-fitting model of the radio-emitting forward shock radius evolution with time reads:

$$R_{\text{FS}}(t) = (6.27 \pm 0.22) \left(\frac{t}{\text{yr}} \right)^{0.77 \pm 0.03} \left(\frac{d_A}{15.1 \text{ Mpc}} \right) 10^{16} \text{ cm} \quad (4)$$

where d_A is the angular diameter distance, which we use 14.7 Mpc (Freedman et al. 2001). The time derivative of Equation (4) implies an FS velocity $v_{\text{FS}} \gtrsim 10,000 \text{ km s}^{-1}$, at the same time we derive a $v_{\text{FS}} \approx 4000 \text{ km s}^{-1}$ from the X-rays, inferred from Equation (3) (for the observed $T \sim 20 \text{ keV}$).¹⁵ This discrepancy suggests that the radio and X-ray observations

¹⁵ We note that the v_{FS} derived from VLBI imaging of SN 2014C is also significantly larger than the value reported by Anderson et al. (2016). We ascribe this difference to the assumption of synchrotron radiation in the self-absorbed regime in the modeling of 15 GHz data of SN 2014C by Anderson et al. (2016), which might not be realistic. In the following, we adopt the direct constraints on the size of the radio-emitting region obtained with VLBI techniques.

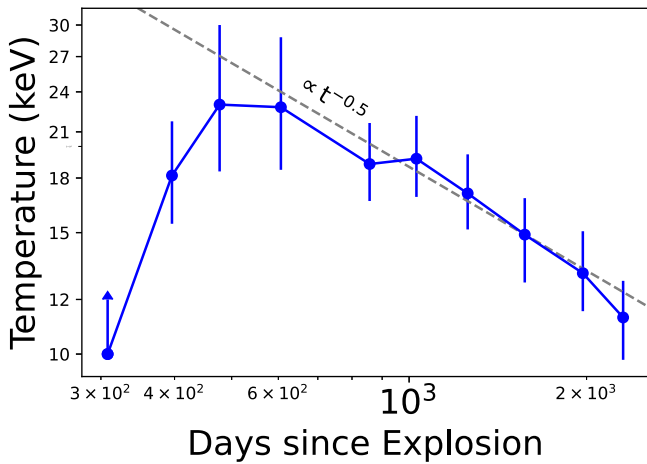


Figure 4. Temperature evolution with time as revealed by our broadband X-ray modeling. From the first CXO observation, Margutti et al. (2017) inferred $T > 10$ keV, which we plot here. The dashed gray line marks a $t^{-0.5}$ power-law decay to guide the eye.

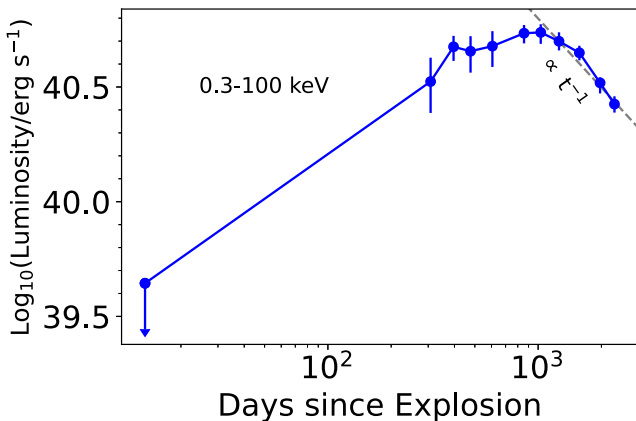


Figure 5. Evolution of 0.3–100 keV X-ray luminosity with time as revealed by our broadband spectral modeling. Very early *Swift*-XRT observations acquired at $\delta t = 7$ –20 days led to $L_x < 4.41 \times 10^{39}$ erg s $^{-1}$ (Margutti et al. 2017). A gray dashed line marks a $\propto t^{-1}$ decay to guide the eye.

are tracing two different emitting regions. Broadly speaking, we expect the radio synchrotron emission to trace the fastest moving material, while X-rays are powered by bremsstrahlung radiation and are therefore expected to trace the densest material (provided that the photons are not absorbed locally by the material).

Additionally, any valid model would need to reconcile two independent and important observational constraints: (i) from VLBI observations, Bietenholz et al. (2021b, 2017) found the emission consistent with a projection of a spherical shell into the sky plane, implying that the fastest moving material is consistent with (albeit can still deviate from) a spherical source; and (ii) a broad $H\alpha$ spectral component with width of a few thousand kilometers per second emerged in the spectra of SN 2014C at 127 days after the explosion, at the same time as the X-ray and radio re-brightening (Milisavljevic et al. 2015; Mauerhan et al. 2018; Thomas et al. 2022). Since the ejecta of SN 2014C are H-poor (SN 2014C was originally classified as a type-Ib SN), following the reasoning of Chugai & Chevalier (2006) for SN 2001em, Margutti et al. (2017) associated the width of the broad $H\alpha$ component with shocked CSM material,

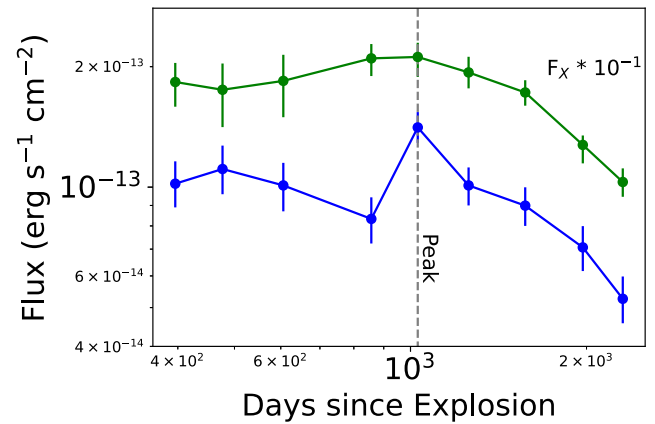


Figure 6. Evolution of the Fe line emission (blue) and total emission (green, rescaled by 10^{-1}) with time to show similarities in overall behavior. The Fe line emission is consistent with no change until $\delta t \approx 850$ days. The line emission starts to decay at $t > 1000$ days along with the X-ray continuum of Figure 5. The equivalent width of the Fe line emission remains roughly constant with time, suggesting a physical connection between the Fe line emission and the continuum emission.

which implies an FS velocity of a few thousand kilometers per second, comparable to the inferred velocity of the X-ray emitting material. This line of reasoning supports the association of the X-ray emitting material with H-rich, dense shocked CSM. Instead, the radio-emitting region imaged by VLBI is located at a larger radius, and the radio-emitting material is expanding at a significantly larger velocity in the environment (i.e., the radio shock traced by VLBI was not as heavily decelerated as the X-ray emitting material).

The inferences from the X-ray, optical, and radio VLBI observations of SN 2014C can be reconciled in a scenario where the CSM is highly asymmetric, e.g., in the shape of an equatorial “disk” as shown in the cartoon in Figure 7. Within the inner disk radius R_i , the expansion of the FS is spherically symmetric, and the FS has the same expansion velocity in all directions. At distances $>R_i$, the FS dynamics are impacted by the presence of the dense equatorial disk of CSM. As a consequence, material ejected along the polar directions will interact with CSM material of significantly lower density than that of the denser CSM on the equatorial plane. We associate the faster, quasi-spherical FS component with the VLBI emitting region (Figure 7), and the significantly decelerated equatorial FS with the X-ray and $H\alpha$ emitting material. Departures from spherical symmetry for the CSM around SN 2014C were initially suggested by Milisavljevic et al. (2015). Additionally, a very similar conclusion has been reached by Thomas et al. (2022) also from the discrepancy between the radio and X-ray velocities.

Within this “disk+quasi-spherical polar outflow” model, prior to the interaction with the CSM equatorial disk at R_i , the FS front was spherical (thick black line in Figure 7) and later was not strongly decelerated as it did not encounter the thick disk. Thus, we extrapolate the position of the shock using the inferences from VLBI imaging (i.e., Equation (4)) to the onset time of strong interaction ($\delta t \sim 100$ days, as constrained by optical spectra from Milisavljevic et al. 2015) and then we use the shock velocities inferred from the X-ray spectral modeling (Equation (3)) to estimate the shock radius evolution with time within the thick disk (Figure 8, blue squares). In this scenario, the CSM inner radius is $R_i \approx 2.2 \times 10^{16}$ cm and the X-ray

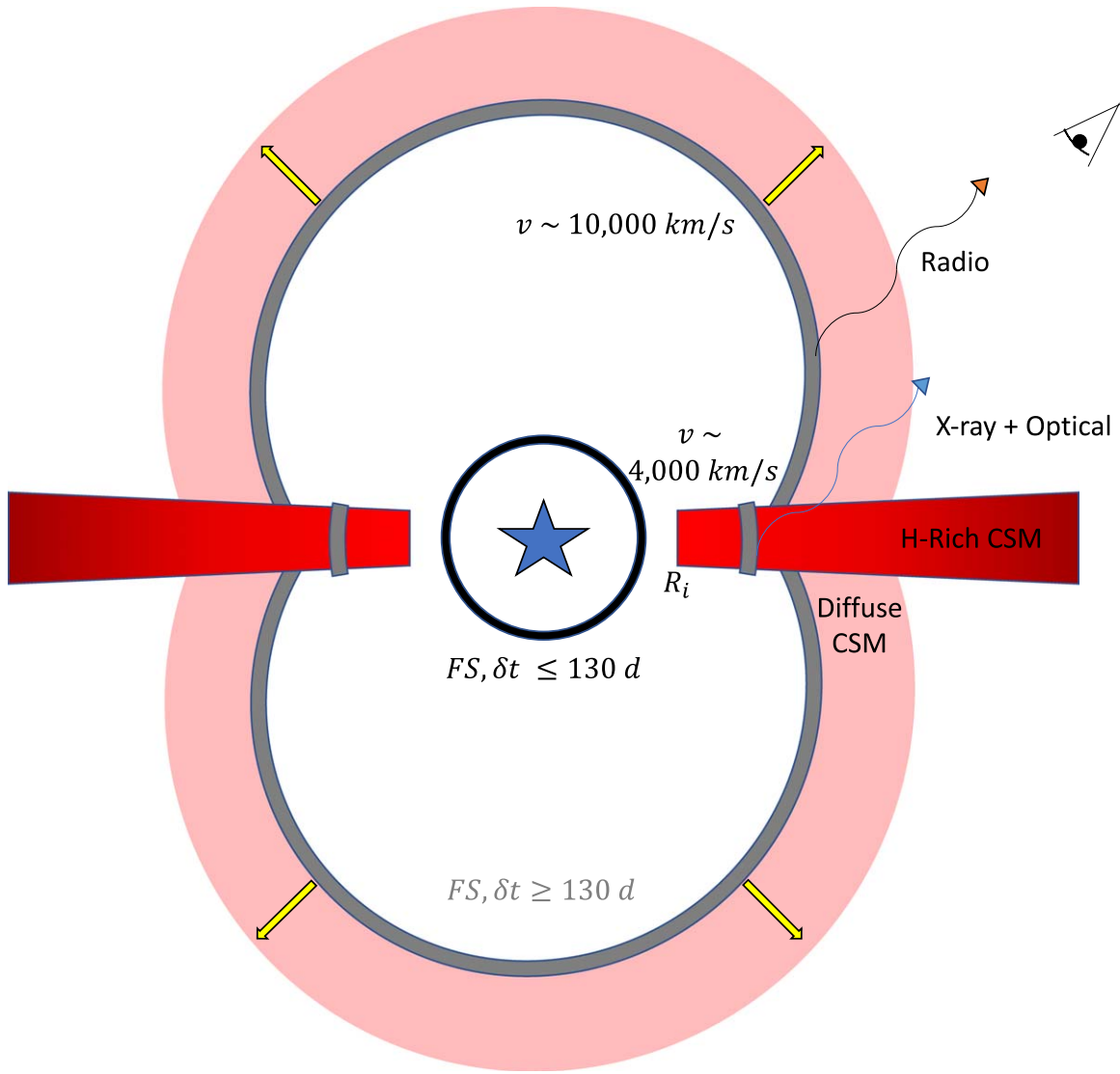


Figure 7. Side view cartoon depiction of the geometry around SN 2014C. The CSM is contained within the equatorial plane, beginning at a radius $R_i \sim 2.2 \times 10^{16}$ cm, which the FS achieved within 130 days post-explosion. Prior to 130 days, the FS was mostly spherical. Upon striking the equatorial CSM, that portion of the FS slowed down from $\sim 10^4$ to $\sim 4 \times 10^3$ km s $^{-1}$. This interaction of FS and CSM generates the observed X-rays, while the FS that was only slightly decelerated by a significantly lower-density medium at $\sim 10^4$ km s $^{-1}$ generates the observed radio emission. As the FS is only impeded in the equatorial plane, the radio emission creates an hourglass shape, which is consistent with the spherical symmetry found by Bietenholz et al. (2021b). A similar geometry has been invoked by Milisavljevic et al. (2015) and, more recently, by Thomas et al. (2022) for the specific case of SN 2014C, and also observationally for other SNe (e.g., Smith et al. 2015; Andrews & Smith 2018; Brennan et al. 2022a) and theoretically in hydrodynamical simulations (e.g., Kurfürst & Krtićka 2019).

observations presented in this paper probe the CSM out to a radius $\sim 10^{17}$ cm at $\delta t = 2307$ days (Figure 8).

3.3. Properties of the CSM Probed by X-Ray Observations

We estimate the total mass and density profile of the CSM probed by X-ray observations (i.e., the “disk” in Figure 7) using two independent methods: the evolution of the $\text{NH}_{\text{int}}(t)$ and $\text{EM}(t)$. We expect both methods to lead to the same order of magnitude estimate of the CSM mass. However, the $\text{NH}_{\text{int}}(t)$ provides a direct measurement of the neutral material (i.e., material that absorbs X-ray radiation through photoelectric effects) along the line of sight, while the $\text{EM}(t)$ depends on the volume and density of the emitting material.

First, we compute the CSM mass constraints inferred from $\text{EM}(t)$. Following Margutti et al. (2017) and our discussion in Section 3.2, we identify the emitting region as the shocked

CSM, which has volume:

$$V_{\text{FS}} \approx 4\pi R^2 \Delta R f \quad (5)$$

where ΔR is the thickness of the FS shocked CSM shell, and f is a filling factor that quantifies the deviation of the shocked material from spherical symmetry. Combining Equation (5) with Equation (2), the density of the shocked CSM is:

$$\rho_{\text{FS}}(t) = \sqrt{\frac{\text{EM}(t) \mu_e^{\text{FS}} \mu_I^{\text{FS}}}{V_{\text{FS}}(t)}} m_p. \quad (6)$$

The density of the CSM upstream is $\rho_{\text{CSM}} \sim \frac{1}{4} \times \rho_{\text{FS}}$ for a shock compression factor $R \sim 4$ appropriate of strong shocks and monatomic ideal gas. Additionally, we assume that only \sim half of the radiation can reach the observer, and so multiply $\text{EM}(t)$ by 2. Assuming that at any time t the X-ray emission is dominated by newly shocked material at radius $R(t)$ in a shell

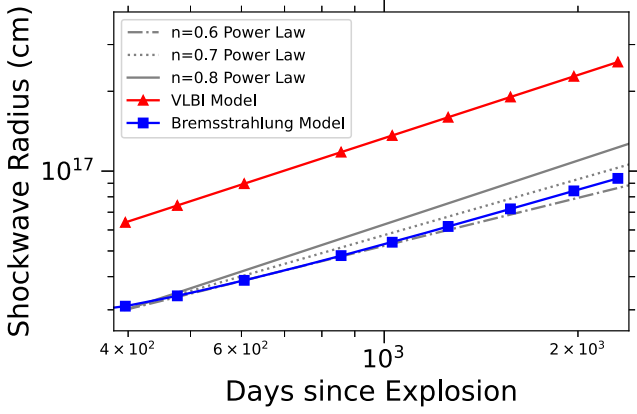


Figure 8. Inferred temporal evolution of the radius of the shockwave that dominates the radio emission detected by VLBI (red triangles, Equation (4) from Bietenholz et al. 2021b), and the inferred radius of the X-ray emitting material (blue squares, Section 3.2) calculated using the shock velocity inferred from Equation (3). The thick, dotted, and dotted–dashed gray lines are the power-law evolution of the radius $R \propto t^n$ with $n = 0.8$, $n = 0.7$, and $n = 0.6$, respectively, to guide the eye.

of shocked material of thickness ΔR ,¹⁶ the resulting pre-shock CSM density is thus given by:

$$\rho_{\text{CSM}}(t) = \sqrt{\frac{EM(t)\mu_e^{\text{FS}}\mu_I^{\text{FS}}}{32\pi R(t)^2 \Delta R f}} m_p. \quad (7)$$

We show our results in terms of shell mass, total shocked mass, mass density, and particle number density in Figures 9 and 10 (blue squares).

Second, we derive constraints on the CSM mass from $\text{NH}_{\text{int}}(t)$. NH_{int} is the column density of the equivalent amount of neutral hydrogen between an observer and the object, and is defined as

$$\text{NH}_{\text{int}} = \int_{R_E}^{R_{\text{obs}}} n_H(r) dr \quad (8)$$

where n_H is the number density of hydrogen, R_{obs} is the distance of the observer from the object, and R_E is the radius at which radiation is produced. The observed difference of $\text{NH}_{\text{int}}(t)$ between two observations carried out at t_1 and t_2 , where $R_E(t_1) \equiv R_1$ and $R_E(t_2) \equiv R_2$ is:

$$\Delta \text{NH}_{\text{int}} = \int_{R_1}^{R_2} n_H(r) dr \approx n_H(R_1) \times (R_2 - R_1) \quad (9)$$

where we assumed that n_H is approximately constant between R_1 and R_2 .

It follows that the total mass the shock has traveled through between two observations at t_1 and t_2 is:

$$\Delta M_{\text{CSM}}(t) = \frac{m_p}{X_H} \left(\frac{\Delta \text{NH}_{\text{int}}(t)}{R_2 - R_1} \right) V_{R_1, R_2}(t) \quad (10)$$

where X_H is the fraction by mass of hydrogen, $V_{R_1, R_2}(t)$ is the spherical volume between R_1 and R_2 (and therefore $V_{R_1, R_2}(t) \propto f$) and $X_H = 0.7381$ for solar abundances (Asplund et al. 2009). We show $\Delta M_{\text{CSM}}(t)$ and the mass sampled by the shockwave as it expands in the CSM in Figure 9, red symbols.

¹⁶ We expect this assumption to break down at late times, i.e., once the shock emerges from the thicker part of the H-rich CSM “disk.”

Finally, we find that the total amount of *neutral* mass sampled by the shockwave between $\delta t = 396$ days to $\delta t = 2307$ days is $M_{\text{CSM}} \approx (1.2 \pm 0.03) f M_{\odot}$.

Similarly, we estimate the mass of the CSM using the density profile from $EM(t)$ (which is sensitive to ionized material emitting free–free radiation) as $M_{\text{CSM}} \approx (2.0 \pm 0.04) \sqrt{f} M_{\odot}$. These two estimates agree within a factor < 2 . We provide the statistical uncertainties from standard error propagation only. However, it is clear that a major source of uncertainty is of systematic nature and related to the geometry of the CSM, which we quantify with the filling factor f , and to the thickness of the shocked region (represented by the ΔR parameter). With these caveats in mind, we find that the best-fitting CSM “disk” density profile scales as $\rho_{\text{CSM}}(R) \propto R^{-1.50 \pm 0.01}$ and $\rho_{\text{CSM}}(R) \propto R^{-2.42 \pm 0.17}$ for the $EM(t)$ and the $\text{NH}_{\text{int}}(t)$ methods, respectively (Figure 10). For $f=1$ and a wind velocity $v_w = 1000 \text{ km s}^{-1}$, the inferred $\rho_{\text{CSM}}(r)$ profiles correspond to very large mass-loss rates in the range $\dot{M} \approx (0.03\text{--}0.1) M_{\odot} \text{ yr}^{-1}$ (Figure 10).

4. Discussion

SN 2014C was initially spectroscopically identified as a type Ib SN and transitioned to a strongly interacting type II_n over ~ 1 yr (Milisavljevic et al. 2015). From our modeling of the evolution of the broadband X-ray emission from SN 2014C, we infer the presence of dense H-rich asymmetric CSM starting at $R_i \approx 2 \times 10^{16}$ cm and with mass in the range $M_{\text{CSM}} \approx (1.2f - 2.0\sqrt{f}) M_{\odot}$, which is consistent with previous estimates by Margutti et al. (2017), Vargas et al. (2022), and Harris & Nugent (2020; see Figure 9). Intriguingly, Harris & Nugent (2020) also note that radio observations at 15.7 GHz indicate a significantly smaller CSM mass than the X-rays ($M_{\text{radio}} \lesssim 0.3 M_{\odot}$ versus $M_{\text{X-ray}} \lesssim 1.5 M_{\odot}$), further supporting a disassociation between the radio and X-ray data. This is due to the conflicting effects within their simulation of the forward shock speed and the density of the CSM shell, where the increase in shock speed at $\delta t \lesssim 400$ days seen in the radio had to be offset by a decrease in shell density in order to accurately reproduce the observed radio light curve. In this section we start by putting the CSM shell parameters of SN 2014C into the broader context of other core-collapse SNe that showed clear signs of shock interaction with a dense medium at some point during their evolution (Section 4.1). Second, we explore in Section 4.2 the physical mechanism(s) that might be behind the mass-loss phenomenology currently observed in core-collapse SNe.

4.1. SN 2014C in the Context of Interacting Core-collapse SNe

We collected from the literature a large sample of 121 core-collapse SNe that showed observational signatures of strong CSM interaction (Table 1). While we recognize that this sample is certainly not complete, the goal of the sample is to provide a synthesis of the multitude of efforts to explore the wide diversity of CSM interaction in the literature of the past couple decades. Shock interaction with a dense CSM can manifest through at least one of the following observational features: (i) spectral narrow lines (transient or persistent) due to shock ionization of wind material ahead of the shock; (ii) photometric variability of the SN light curve (including multiple bumps); and/or (iii) luminous X-ray/radio emission.

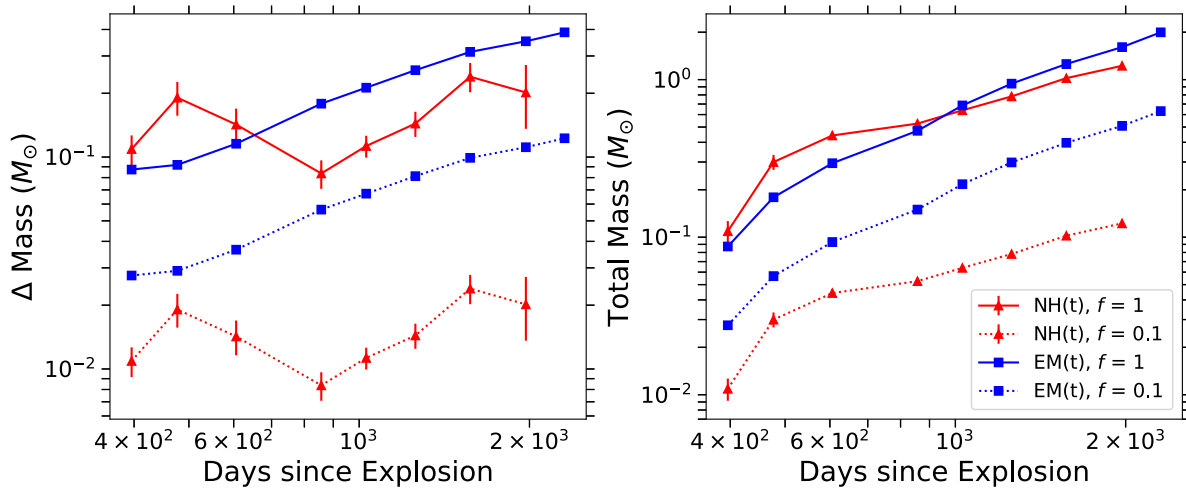


Figure 9. Incremental mass added between observations (left) and total mass (right) based on $\text{NH}_{\text{int}}(t)$ (red triangles) and $\text{EM}(t)$ (blue squares). The $\text{NH}_{\text{int}}(t)$ masses are calculated via Equation (10) using radii from X-ray emission, while the $\text{EM}(t)$ masses are calculated using Equations (5) and (6) under an assumption that shell thickness is $0.1R$. Importantly, each measurement of accumulated mass from $\text{NH}_{\text{int}}(t)$ requires a following observation; hence, there is one fewer data point compared to the $\text{EM}(t)$. The nonsolid lines represent a filling factor of 0.1 applied to each method, as estimated by line emission in Milisavljevic et al. (2015). We note that the plotted error bars reflect statistical uncertainties only (statistical uncertainty of $\text{EM}(t)$ is smaller than the squares).

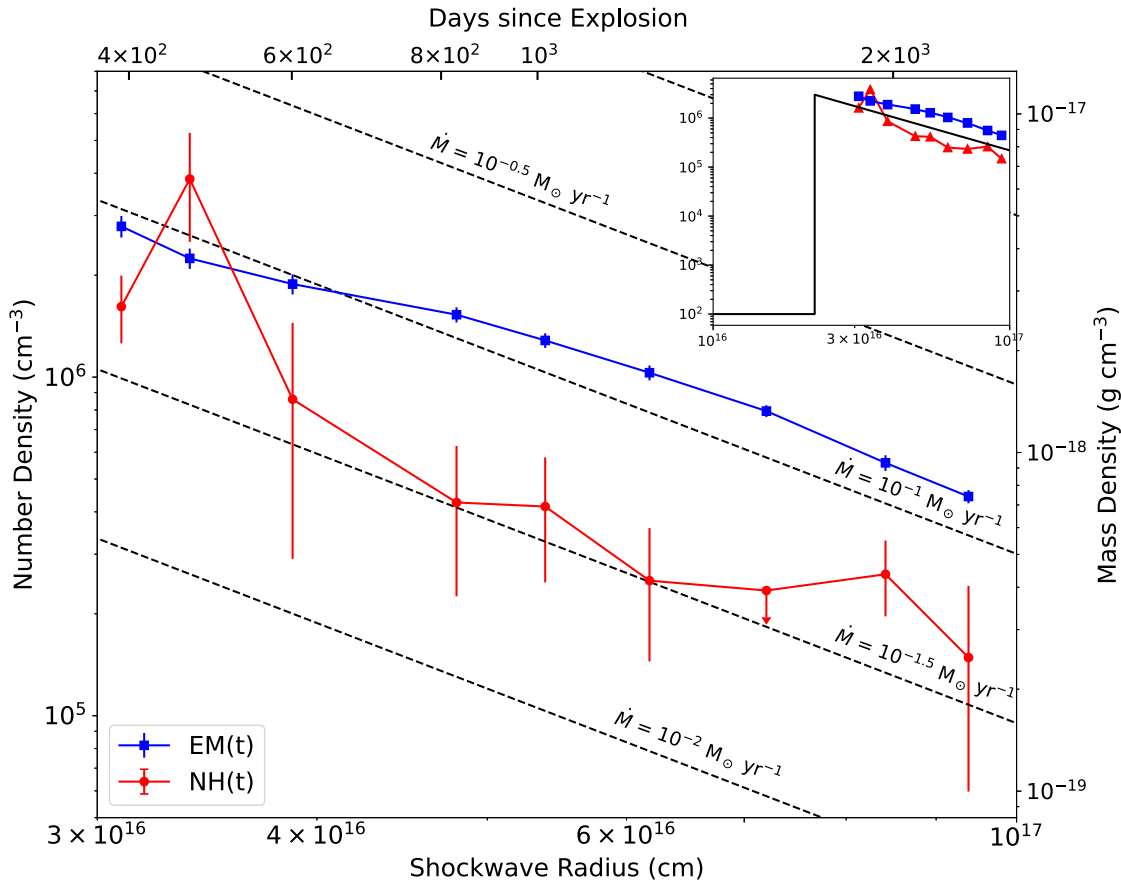


Figure 10. Density profile of the CSM assuming solar chemical composition, as derived from $\text{NH}_{\text{int}}(t)$ (red triangles) and $\text{EM}(t)$ (blue squares) following the assumptions stated in Section 3.3. We assume $f=1$, $\Delta R = 0.1R(t)$, $\mu_e = 1.25$, and $\mu_l = 1.15$ in these calculations. Black dashed lines: wind-density profiles for a range of mass-loss rates \dot{M} , i.e., $(\rho_{\text{CSM}} = \dot{M}/(4\pi v_w R^2))$ for $\log(\dot{M}/M_\odot \text{ yr}^{-1}) = [-2, -1.5, -1, -0.5, 0]$ with an assumed wind speed of $v_w = 1000 \text{ km s}^{-1}$. Due to a small change in NH_{int} between observations for $\sim 7 \times 10^{16} \text{ cm}$, the point is an upper limit as the error bars are approximately equal to the density measurement. Fitting with a power law, the density profile is best fit with $\rho_{\text{CSM}} \propto R^{-2.42 \pm 0.17}$ and $R^{-1.50 \pm 0.01}$, derived from $\text{NH}(t)$ and $\text{EM}(t)$, respectively. Both profiles are inconsistent with a wind profile, albeit with an extreme mass-loss rate. We note that the plotted error bars reflect statistical uncertainties only.

Table 1
Sample of Strongly Interacting Core-collapse SNe

	H-rich CSM	H-poor CSM
H-rich Ejecta	<p>IIn</p> <p>1996cr, 1987F, 1988Z 1994W, 1994aj, 1995G 1995N, 1996L, 1997ab 1997eg, 1998S, 2005gl 2005ip, 2005kj, 2006aa 2006bo, 2006jd, 2006qq 2006tf, 2008fq, 2008iy, 2009ip^a, 2010jl, 2010mc 2011fh, 2011ht, 2013L 2015 da, 2016jbu</p> <p>IIP/L</p> <p>1996al, 1999em, 1999gi 2001X, 2003Z, 2003hn 2004et, 2005cs, 2006Y 2006ai, 2007od, 2009N 2009ib, 2009kf, 2011ja iPTF11iqb, 2012A, 2012aw 2012ec, 2013ab, 2013by 2013ej, 2013fs, PS1-13arp LSQ13dpa, 2014cy, ASASSN-14dq ASASSN-14gm, ASASSN-14 ha, iPTF14hls 2016egz, 2017eaw, 2017gmr 2018zd, 2020faa, 2020pni 2020tlf</p> <p>Type II SLSNe</p> <p>2006gy, 2008es, 2016aps 2017hcc</p> <p>Type II</p> <p>1987A, 2017ahn</p>	?
H-poor Ejecta	<p>14C-like Events</p> <p>2001em, 2004dk, PTF11qjc 2014C, 2017dio, 2017ens 2019oys, 2019yvr</p> <p>Ib</p> <p>1993J, 2004C, 2011dh 2013cu, 2013df, 2018gix ASASSN-15no^b</p> <p>Type I SLSNe</p> <p>PTF10aagc, iPTF13ehe, iPTF15esb iPTF16bad, 2017ens</p>	<p>Ibn</p> <p>1999cq, 2002ao, 2006jc 2010al, 2011hw, OGLE-2012-SN-006 LSQ13ddu, 2014av, ASASSN-14ms 2019uo</p> <p>Icn</p> <p>2010mb, 2019jc, 2019hgp 2021ckj, 2021csp</p> <p>Type I SLSNe iPTF16eh</p> <p>Type Ib/c</p> <p>2003gk, 2004cc, 2004gq 2012aa, LSQ14efd, iPTF15dtg 2016iet, 2018gep, 2018ijp 2019cad, 2019ehk, 2020oi 2020bv</p>

Notes. See Appendix A for references.

^a SN 2009ip refers to the 2012 explosion.

^b ASASSN-15no interacted with H-poor material. ASASSN-15no was spectroscopically classified as a type Ic at early times (Balam & Graham 2015), then later reclassified as type II (Benetti et al. 2018).

The core-collapse SN interacters fall into three major physical categories based solely on the composition of the ejecta and that of the CSM (Table 1):

1. *Group 1: SNe with H-poor ejecta interacting with dense, H-rich CSM.* Type Ib and type Ic SN 2014C-like transitional objects and SLSNe-I with late H α emission belong to this group.
2. *Group 2: SNe with H-poor ejecta interacting with H-poor CSM.* Belonging to this group are type Ibn SNe and the recently identified class of type Icn SNe, as well as type Ib/c SNe that interacted with H-poor CSM without producing narrow spectral lines.
3. *Group 3: SNe with H-rich ejecta interacting with dense, H-rich CSM.* Belonging to this group are normal type IIn SNe and SLSNe IIn, UV-bright type IIP/IIL SNe, and interacting type IIP/IIL SNe.

The physical parameters of interest for our study are: (i) the onset time and the end time of the interaction t_{start} and t_{end} , respectively; (ii) the location of the dense CSM parameterized by an inner and outer radius of the CSM, R_{in} and R_{out} , respectively; the total CSM mass M_{CSM} ; (iii) the wind velocity v_w (i.e., the ejection velocity of what later becomes CSM); (iv)

and the implied mass-loss rate, \dot{M} , assuming a wind profile. When possible, we calculated (or retrieved) the values of these parameters using the information provided in the papers referenced in Table 1. Our detailed reasoning for each SN is reported in Appendix A for the reader to be able to fully reproduce our results and figures. We explicitly state what type of data the parameters were derived from in Tables 7 and 8 as each method has its own biases.

Before commenting on the results from this exercise (displayed in Figures 11, 12, and 13), we emphasize that the physical parameters have been estimated with a variety of observational “tracers.” This is particularly true for the CSM mass for which various methods are known to lead to different estimates. Again, our collected sample of interacting core-collapse SNe represents the status quo of the field, but it is hardly complete nor homogeneous. The goal is to illustrate the variety of CSM properties that have been claimed in the literature so far.

With the above caveats in mind, we find that our heterogeneous sample of core-collapse SNe showed CSM interaction over a large dynamic range of times since explosion (from time of first light until several 1000 days; Figure 11), which maps onto a large dynamic range of distances from the

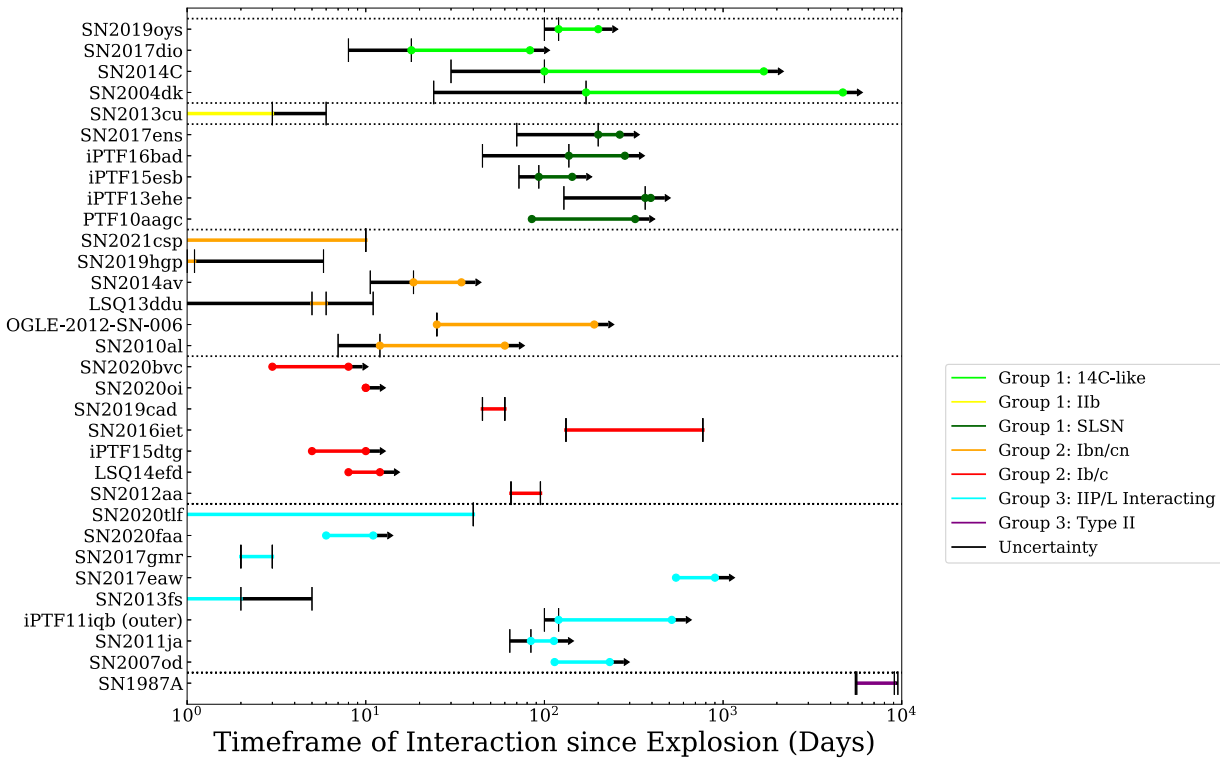


Figure 11. A comparison of the time frames of interaction using the same color scheme as in Figures 12 and 13 (the legend also reflects the order that categories appear). Most points are lower limits, as interaction was still ongoing as of the latest observation when the transient faded below the threshold of detection. Uncertainties in interaction onset are dominated by the time between consecutive observations. Type IIcn SNe are included only in Tables 7 and 8 due to assumptions and uncertainties in their properties. Circles represent when the data include a lower limit.

explosion site $\sim 3 \times 10^{13} - 10^{18}$ cm (Figures 12, 13). The range of inferred CSM masses is also broad, with M_{CSM} spanning $\sim 10^{-4} M_{\odot}$ up to tens of M_{\odot} of material (Figure 13). The large dynamic ranges of these key parameters likely reflect the diversity of stellar progenitors (and hence ejection velocity and composition of the CSM material) as well as a variety of envelope mass ejection mechanisms that we discuss in more detail in Section 4.2.

Below we comment on some specific types of SN interactors that are directly relevant to SN 2014C. While we show interacting type IIP SNe for completeness in Figures 11, 12, and 13, their H-rich red supergiant (RSG) stellar progenitors (Smartt 2015) as well as difference in ejected mass likely imply mass ejection mechanisms different from those at play in the more compact H-poor evolved massive stars.

4.1.1. SN2014C-like Type Ib/c SNe

The same finding of a large dynamic range of CSM distances and masses holds even restricting the sample to core-collapse SNe from H-poor progenitors (like SN 2014C) that also showed evidence for interaction with CSM of different chemical composition and geometries. The transition from type Ib/c to type IIn SN due to H-rich CSM interaction has been reported in at least 11 SNe so far, i.e., SNe 2001em (Soderberg et al. 2004), 2004dk (Mauerhan et al. 2018), iPTF11qej (Corsi et al. 2014), iPTF13ehe (Yan et al. 2017), 2014C (Milisavljevic et al. 2015), iPTF15esb (Yan et al. 2017), iPTF16bad (Yan et al. 2017), 2017dio (Kuncarayakti et al. 2018), 2017ens (Chen et al. 2018), 2018gix (Prentice et al. 2020), and 2019yvr (Kilpatrick et al. 2021) while interaction with an H-poor medium has been invoked for SNe 2012aa

(Roy et al. 2016), 2019ou (Strotjohann et al. 2021), 2004cc (Wellons et al. 2012), 2004gq (Wellons et al. 2012), iPTF15dtg (Jin et al. 2021), and 2020bvc (Jin et al. 2021). We note that for SNe 2004gq, iPTF15dtg, and 2020bvc, the composition of the CSM was not spectroscopically verified. Most of these SNe show clear signs of interaction between 10 and 100 days after explosion (Figure 11), corresponding to a typical CSM radius $\sim 10^{16} - 10^{17}$ cm (Figure 12), but otherwise display largely different CSM properties. For example, SN 2004dk is an SN2014C-like event for which thick H-rich CSM was inferred to be present starting as close as $\sim 5 \times 10^{15}$ cm and with densities $\sim 2 \times 10^4 \text{ cm}^{-3}$ (i.e., ~ 100 times less dense than in SN 2014C; Mauerhan et al. 2018).

In addition, while here we focus on the small sample of interacting type Ib/c SNe, it is worth noting that the vast majority of type Ib/c SNe do *not* show evidence for interaction with a thick CSM medium for years of radio monitoring after explosion (e.g., Margutti et al. 2017), which implies that most type Ib/c stellar progenitors do not experience substantial mass-loss for $\sim 10^3 - 10^5$ yr prior to explosion depending on the assumed v_w . A large sample study of radio Ib/c SNe by Bietenholz et al. (2021a) infers a typical mass-loss rate $\dot{M} = 10^{-5.4 \pm 1.2} M_{\odot} \text{ yr}^{-1}$ due to stellar winds, which is significantly smaller than in SN2014C-like events, which require $\dot{M} \approx (0.03 - 0.1) M_{\odot} \text{ yr}^{-1}$ (Figure 10). The diversity of CSM properties close to the explosion’s site can be an indication of very different mass-loss mechanisms at play or of the wildly different timescales over which the same mass-loss mechanism can operate in H-poor SN stellar progenitors (e.g., Margutti et al. 2017). While stellar winds may account for extended and tenuous CSM, binary interaction may account for

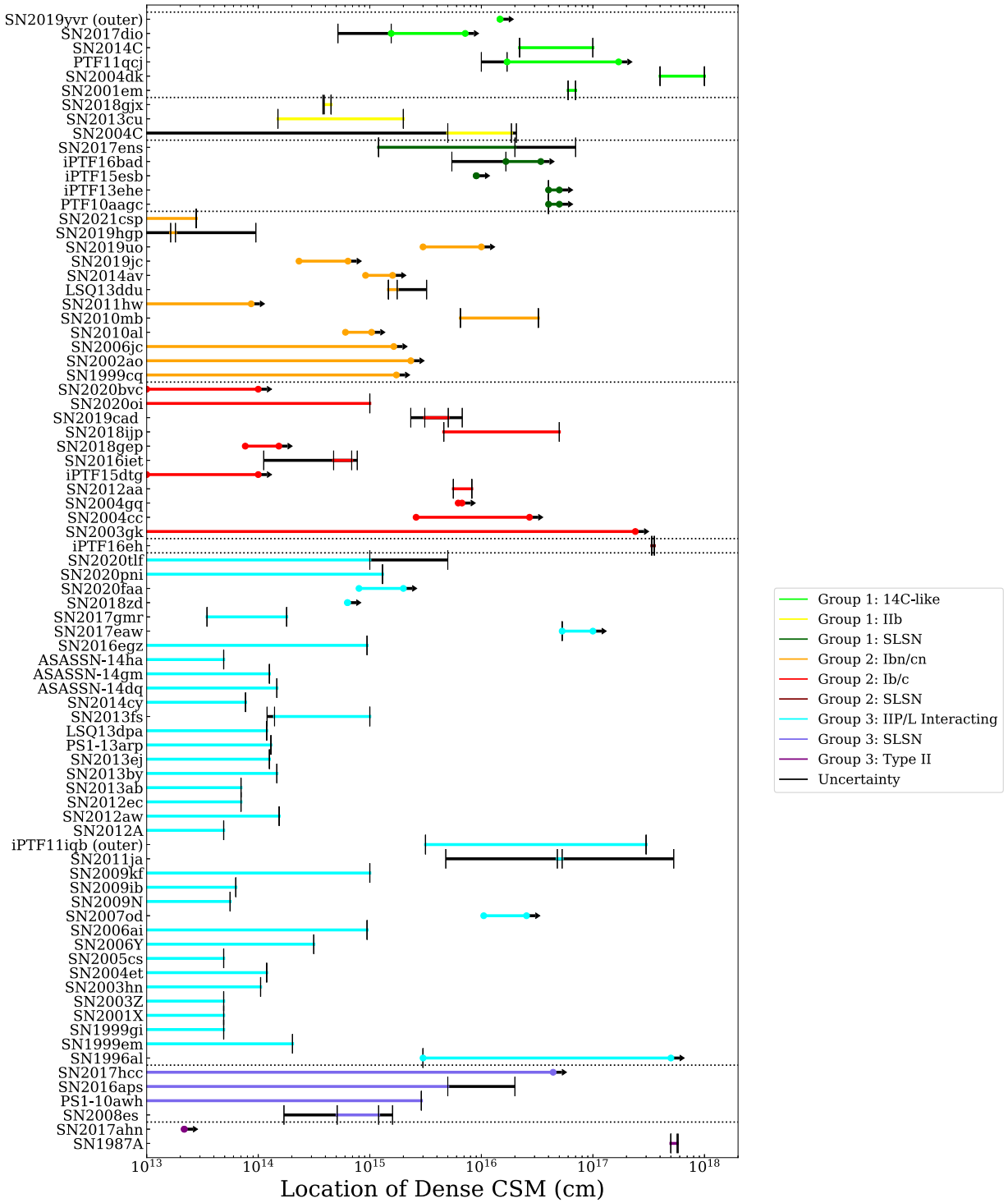


Figure 12. Radial location (or extension) of the regions of high-density material for different types of SNe that showed evidence for CSM interaction at some point during their evolution. Type II_n SNe are included only in Tables 7 and 8 due to assumptions and uncertainties in their properties. This figure uses the same color scheme as Figures 11 and 13 (the legend also reflects the order that categories appear). Circles represent when the data includes a lower limit.

the high variation in the density of the CSM and distance from the progenitor star.

4.1.2. Type Ibn and Icn SNe

Known types of H-poor SNe interacting with an H-poor medium include type Ibn and type Icn SNe. For type Ibn SNe, the CSM is He-rich (e.g., Pastorello et al. 2008), while for the

recently discovered type Icn SNe, the CSM is both H- and He-poor (and show instead prominent narrow emission of oxygen and carbon from the CSM, e.g., SNe 2021csp, 2021ckj, 2019hgp, and possibly 2010mb; Fraser et al. 2021; Gal-Yam et al. 2021; Pellegrino et al. 2022; Perley et al. 2022). These SNe represent the case of stripped progenitors interacting with material that was lost from inner layers, i.e., after H-envelope removal. Interestingly, the inferred location of this H-poor

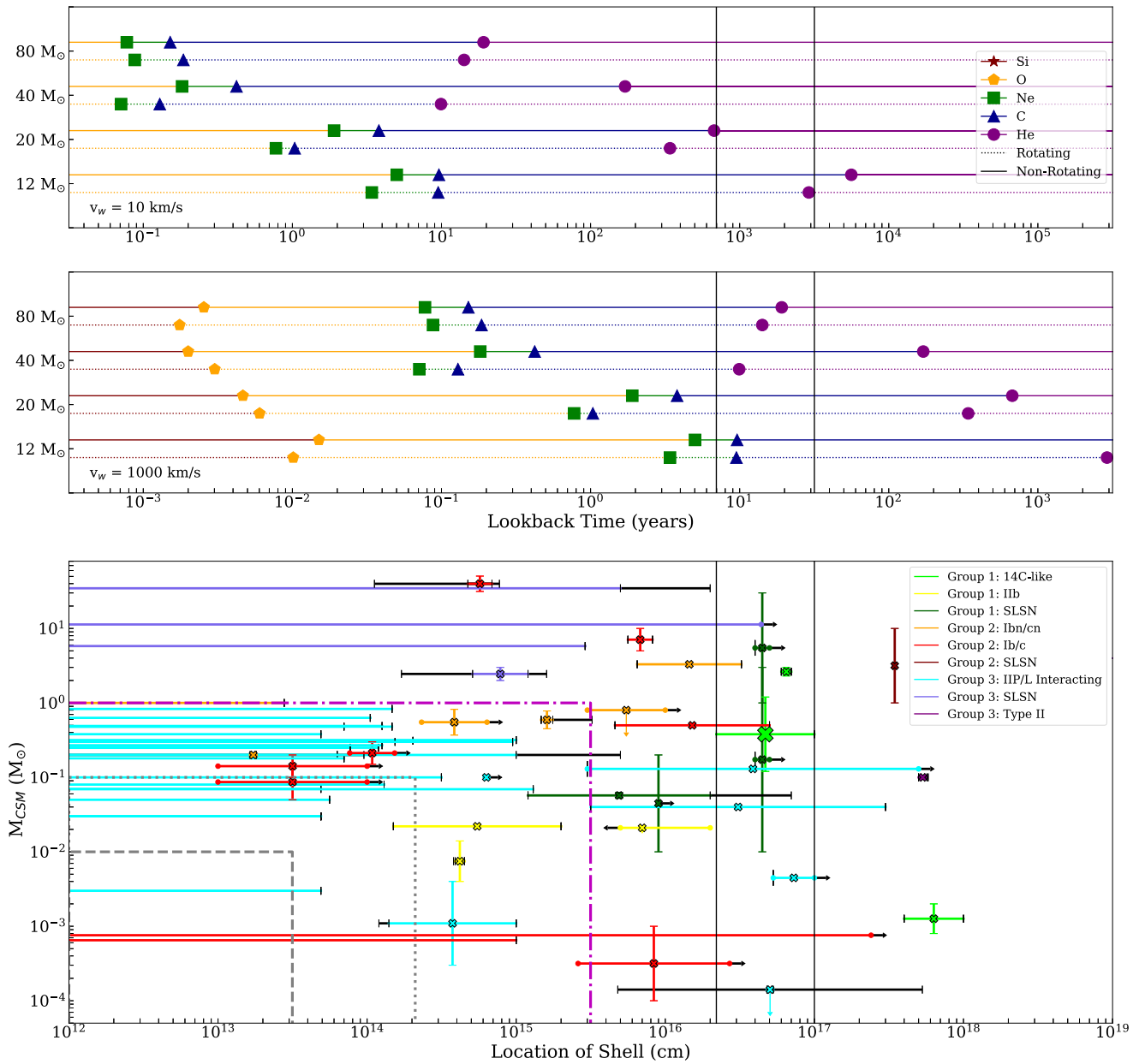


Figure 13. Upper and middle panels: core nuclear burning stages of massive stars with $M = 12\text{--}80 M_{\odot}$ as a function of time before collapse. Solid and dotted lines represent nonrotating and rotating stars with $\Omega = 0.5$, as described in Shiode & Quataert (2014), respectively. Lower panel: amount of mass lost plotted against the location of the thick CSM for a subset of SNe in Figure 12 and follows the same color scheme. The x-axis of this plot maps into the x-axes of the middle and upper panels for an assumed wind speed of 10 km s^{-1} (top panel) or 1000 km s^{-1} (middle panel). Vertical black solid lines emphasize the location of the CSM material for SN 2014C. For the CSM mass of SN 2014C, we use an upper limit of $f = 1$ and a lower limit of $f = 0.1$. Additionally, we show the boundaries for which three wave-driven mass-loss episodes occurred in simulations. The magenta dotted-dashed line represents a Wu & Fuller (2021) model, and the gray dotted and dashed lines represent an H-rich and H-poor model from Leung et al. (2021b). Details of the model are described in Section 4.2.

material and its mass also span large ranges: up to few M_{\odot} of material (e.g., $M_{\text{CSM}} \sim 1 M_{\odot}$ and $M_{\text{CSM}} \sim 3.3 M_{\odot}$ for SNe 2021csp and 2010mb, respectively; Ben-Ami et al. 2014; Fraser et al. 2021), extending from the stellar surface to $>10^{16} \text{ cm}$.

These scenarios are indicative of an H-poor equivalent to 14C-like events with delayed interaction, albeit typically at earlier times and for a shorter duration, as well as with higher wind velocities of $\sim 1000 \text{ km s}^{-1}$ (e.g., Pellegrino et al. 2022). This may suggest that type Ib/cn events exist at the extreme end of the spectrum of mass-loss events where the mass-loss event was initiated at very late times.

4.1.3. SLSNe

One potential explanation for the large luminosities of SLSNe (e.g., Chomiuk et al. 2011; Quimby 2012; see Gal-Yam 2019 for a recent review) is efficient kinetic energy conversion into radiation due to shock interaction with a thick medium. Within this scenario, extreme mass-loss histories have been invoked to power the persistent, luminous displays that are typical of SLSNe. For example for the type IIcn SLSNe 2006gy (Ofek et al. 2007; Smith et al. 2008b; Fox et al. 2015) and 2016aps (Nicholl et al. 2020; Suzuki et al. 2021) and the H-stripped SLSNe 2016iet (Gomez et al. 2019) and iPTF16eh (Lunnan et al. 2018), several M_{\odot} of CSM material have been

inferred (Figure 13). These dense regions of CSM are typically located at distances far from the progenitor at $\sim 10^{16}$ cm and often extending far beyond to $\sim 10^{17}$ and even to $\sim 10^{18}$ cm, implying mass ejections that occurred on timescales of hundreds to tens of thousands of years prior explosion.

Within interacting SLSNe, the most relevant comparisons to the phenomenology of SN 2014C are SLSNe-I for which H α emerged at late times, presumably from the SN shock interaction with H-rich material, as seen in iPTF13ehe, iPTF15esb, and iPTF16bad (Yan et al. 2017) as well as SN 2017ens (Chen et al. 2018). The typical time of interaction onset is approximately hundreds of days, with uncertainty driven by the time between spectra (see Figure 11). Intriguingly, the estimated CSM mass for these events ranges from 0.05 to $3 M_{\odot}$, which is broadly similar to our calculations of SN 2014C’s shell and of a similar timescale.

4.1.4. Type IIn

Finally, we comment on type IIn SNe (Schlegel 1990), as they might represent extreme cases of 14C-like events where the mass ejection occurred just before stellar core collapse, as was suggested, for example, for SN 1996cr (Dwarkadas et al. 2010). The link between LBV progenitors and type IIn, e.g., SN 2005gl (Gal-Yam et al. 2007), SN 2009ip (Mauerhan et al. 2013; Margutti et al. 2014; Smith et al. 2016), and SN 2010mc (Ofek et al. 2013), can explain the rarity and associated mass ejections.

In this scenario there might be a continuum of properties between at least some ordinary type IIn SNe, 14C-like SNe and ordinary type Ib/c SNe, as was suggested by Margutti et al. (2017). Type IIn SNe are typically associated with large inferred mass-loss rates $\dot{M} \sim (0.0001\text{--}0.3) M_{\odot} \text{ yr}^{-1}$ (Kiewe et al. 2012), not dissimilar to our findings for SN 2014C. However, differently from SN 2014C, interaction with an H-rich CSM is detected from the very beginning (indicating the presence of thick CSM all the way to the progenitor surface). Additionally, there are many type IIn SNe that fade below the detection level before the H α emission subsides, providing a lower limit to the radial extent of the H-rich thick CSM, and some for which the H α is observed to vanish before the SN itself fades (e.g., Taddia et al. 2013). Lower limits on the radial extent of the CSM range from $\sim 10^{15}$ cm to more than $\sim 3 \times 10^{17}$ cm, indicating an extensive time range over which the stellar progenitors were experiencing substantial mass loss.

4.2. Mass-loss Mechanisms

We discuss in this section a variety of mass-loss mechanisms and their applicability to the specific case of SN 2014C, as well as to the broader range of observational constraints on mass loss from evolved massive stars of the previous section. Specifically, we discuss in Section 4.2.1 the interaction of the fast Wolf–Rayet (WR) winds and slower RSG winds from the previous evolutionary phase; in Section 4.2.2 binary interaction and mass transfer through Roche lobe overflow and common envelope; and in Section 4.2.3 the complete ejection of the H-envelope triggered by nuclear burning instabilities or gravitational waves. While we discuss these mechanisms separately, this does not indicate that each mechanism is expected to operate independently of one another. In fact, it is anticipated that the mechanisms can interact with one another, such as gravity waves leading to the onset of binary interaction

(Mcley & Soker 2014; Wu & Fuller 2022). We emphasize these three mechanisms because of their ability to explain various aspects of observed mass loss, such as timing and severity of the mass-loss event, in SN 2014C as well as in other events listed in Table 1. However, we recognize this does not represent an exhaustive list of all mass-loss mechanisms.

4.2.1. RSG Wind—WR Wind Interaction

A first possibility is that the progenitor of SN 2014C experienced typical line-driven wind mass loss during an RSG phase. For RSGs, v_w of a few tens of kilometers per second, typical mass-loss rates are $\dot{M} \approx 10^{-6} - 10^{-5} M_{\odot} \text{ yr}^{-1}$ reaching $\dot{M} \approx 10^{-3} M_{\odot} \text{ yr}^{-1}$ in more extreme cases (e.g., de Jager et al. 1988; Marshall et al. 2004; van Loon et al. 2005). The RSG phase was then followed by an anomalously short WR phase, during which winds have typical v_w of a few thousand kilometers per second with $\dot{M} \sim 10^{-5} M_{\odot} \text{ yr}^{-1}$ (e.g., Crowther 2007). The stellar progenitor then exploded as a type Ib SN in the bubble generated by its own WR winds against its previous phase of RSG winds. The ejecta traveled freely for approximately 130 days until they impacted and began to strongly interact with the hydrogen shell producing the transition from type Ib to type IIn.

The interaction between the lighter, faster WR winds with the slower, thicker RSG winds is known to lead to the formation of “shell-like” overdensity structures in the CSM around stars (Dyson 1989). However, the documented cases of WR-RSG wind–wind interaction are associated with “bubbles” at typical distances of $\sim 10^{19}$ cm (Marston 1997), significantly farther than the few 10^{16} cm distances inferred for SN 2014C. In this context, the proximity of the H-rich CSM shell in SN 2014C implies an extremely short WR phase with duration of $\sim 3.5 \left(\frac{v}{2000 \text{ km s}^{-1}} \right)^{-1} \text{ yr}$, conflicting with the $\sim 10^5$ yr duration of the WR phase expected in the case of isolated massive stars, similar to what we concluded in Margutti et al. (2017). We thus explore alternative scenarios. This conclusion extends to all H-poor SNe interacting with H-rich shells at $\leq 10^{16}$ cm, for which an even shorter WR phase would have to be invoked (Figure 13). In the broader context of mass loss in evolved massive stars, the sizes of typical wind-driven bubbles are potentially consistent only with the farthest out CSM shells observed around the SN interacters of our sample.

4.2.2. Binary Interaction

A second possibility is that the progenitor of SN 2014C underwent stripping due to a binary companion. It is well understood that the hydrogen-rich envelope can be lost through binary interaction (e.g., Podsiadlowski et al. 1992), and the majority ($\sim 69\%$) of young massive stars live in interacting binary systems (Sana et al. 2012). Modeling archival pre-explosion Subaru and HST images at the location of SN 2014C, Milisavljevic et al. (2015) found evidence for a massive star cluster with favored age of ~ 30 Myr, and a turn-off mass of the stellar population between 3.5 and $9.5 M_{\odot}$, thus indicating a massive progenitor in the low-mass bin of stars that experience core collapse. Consistent with this finding, Sun et al. (2020) inferred for SN 2014C a progenitor mass of $11 M_{\odot}$ and suggest a binary model where the primary star experienced envelope stripping by the companion, likely through either Case C or Case BC mass transfer then followed by an eruption event or strong metallicity-dependent winds (we refer the

reader to Sun et al. 2020 for further details). We also note that binary interaction is likely to naturally lead to an asymmetric CSM distribution in the environment (e.g., a disk or torus; Ivanova et al. 2013), which is consistent with our inferences of Section 3.2 and Figure 7.

While binary interaction is a viable option for SN 2014C, from a population perspective, we expect 14C-like events due to binary interaction to be quite rare in the last ≤ 1000 yr of a massive star life (Margutti et al. 2017).¹⁷ Despite a large fraction of young massive stars that are in interacting binary systems (Sana et al. 2012), the interaction is not necessarily synchronized with stellar death of the primary star. If binary interaction occurs too early and strips the progenitor of its hydrogen envelope, the CSM produced will be too far away to generate detectable signs of interaction by the time of explosion.

In the broader context of mass-loss events in our sample of SN interacters, binary interaction may be the cause of the wide diversity in CSM distances due to its lack of direct synchronization with stellar death.¹⁸ However, we note that the abundance of type IIP SNe with thick CSM at such close proximity to their progenitor site (Figure 13) and the recent detection of a pre-SN outburst (Jacobson-Galán et al. 2022b) suggests a separate mass-loss mechanism that is timed with core-collapse.

4.2.3. Nuclear Burning Instabilities and Gravity Waves

Eruptive mass loss in the final stages of evolution in massive stars in massive stars can be consistent with nuclear burning instabilities and gravity waves, especially during O and Ne burning, in the few months to years prior to core collapse (Arnett & Meakin 2011; Quataert & Shiode 2012; Shiode et al. 2013; Shiode 2013; Smith & Arnett 2014; Woosley & Heger 2015; Morozova et al. 2020). Specifically, energetic gravity waves are driven by vigorous convection during the last ~ 10 yr of a massive star’s life and have the potential to deposit energy into the envelope and unbind material as originally proposed by Quataert & Shiode (2012). Numerous simulations have attempted to resolve the last years of progenitors ranging from 10–80 M_{\odot} and have become increasingly sophisticated with time (e.g., Leung et al. 2021b; Wu & Fuller 2021, 2022).

For lower-mass stars, which is likely to be the case for the progenitor of SN 2014C as detailed by Milisavljevic et al. (2015) and Sun et al. (2020), Wu & Fuller (2021) identified an 11 M_{\odot} RSG model capable of ejecting $\sim 1 M_{\odot}$ of CSM approximately 10 yr prior to explosion at a velocity of 100 km s⁻¹ (magenta dotted-dashed outline in bottom panel of Figure 13). Similarly, Leung et al. (2021b) found an H-poor model that was able to eject $\sim 0.01 M_{\odot}$ out to $\sim 3 \times 10^{13}$ cm (gray dashed line in the bottom panel of Figure 13). An H-rich progenitor counterpart in the same study was able to eject $\sim 0.1 M_{\odot}$ out to $\sim 2 \times 10^{14}$ cm (gray dotted line in bottom panel of Figure 13).

Both Leung et al. (2021b) and Wu & Fuller (2021) showed that there is strong scatter in their simulations among the

amount of energy (and therefore mass ejected) and the timing of ejection, indicating that the simulations are highly sensitive to input parameters. However, updated simulations from Wu & Fuller (2022) suggest that wave-driven mass loss might be significantly weaker than previously estimated, and might instead be unable to remove more than $\approx 10^{-6} M_{\odot}$ of material. Furthermore, for the specific case of H-stripped progenitors, Wu & Fuller (2022) found that instead of unbinding material, the energy deposited by gravity waves leads to an envelope inflation up to a factor ≈ 10 in radius, which could trigger binary interaction specifically within the last decade of a star’s life. H-rich progenitors, such as RSGs, experience only minor variations in surface properties and are not expected to initiate binary interaction.

It is clear from Figure 13 that gravity waves are insufficient at explaining CSM beyond $\sim \text{few} \times 10^{15}$ cm, even with the more optimistic models from Wu & Fuller (2021) and Leung et al. (2021b). Even before the updated models of Wu & Fuller (2022), it was clear that gravity waves were unable to transfer a sufficient energy to unbind the CSM mass estimated for type IIP events by roughly an order of magnitude for many cases, indicating a large discrepancy between observation and current theory.

There are other mass-loss mechanisms that could be responsible for this discrepancy such as silicon deflagration (Woosley & Heger 2015) or nuclear burning instabilities (Arnett & Meakin 2011), both of which are synchronized with stellar death, or an extended effervescent zone model (Soker 2021).

5. Conclusion

Observations of SNe in recent years have demonstrated our inadequate understanding of how mass loss proceeds in evolved massive stars in the centuries to years before core collapse (e.g., Smith 2014). Here we presented the analysis of data from our broadband hard and soft X-ray campaign of SN 2014C with the CXO and NuSTAR extending from $\delta t = 396$ days to $\delta t = 2307$ days. While the number of SNe with evidence for interaction with a thick CSM is rapidly growing, SN 2014C is still *the only* event for which we were able to detect broadband soft and hard X-ray emission over a timescale of several years. We interpreted this unique set of observations in the context of an absorbed thermal bremsstrahlung radiation model, and we constrained key physical parameters of the emission and their temporal evolution such as emission temperature $T(t)$, intrinsic absorption $\text{NH}_{\text{int}}(t)$, and luminosity output $L_{\text{x}}(t)$. We used the evolution of these parameters with respect to time to infer important parameters of the system, particularly the density profile of the CSM at subparsec scales around the progenitor.

Similar to what we found in Margutti et al. (2017), we find that SN 2014C exploded in a low-density cavity extending to a radius of $\sim 2 \times 10^{16}$ cm. Beyond this radius we find evidence for a high-density CSM with number density $\sim 10^6$ cm⁻³ and neutral density profile not too dissimilar from a wind-like medium, $\rho_{\text{CSM}} \propto R^{-2.42 \pm 0.17}$ (Figure 12). This CSM is hydrogen rich (Milisavljevic et al. 2015; Mauerhan et al. 2018). Furthermore, we find that the combination of the results from the radio monitoring of Bietenholz et al. (2021a) and Bietenholz et al. (2021b) and our broadband X-ray monitoring can be explained in the context of a highly asymmetric CSM with a “disk-like” geometry (Figure 7). Quantifying the

¹⁷ Unless the last phases of stellar evolution are coupled with substantial envelope inflation, e.g., as a consequence of wave heating in H-poor stars (Wu & Fuller 2022) or nuclear burning instabilities (Smith & Arnett 2014).

¹⁸ Note that the underdensity of events beyond $\sim 10^{17}$ cm is likely the result of observational selection effects. Material at those distances is difficult to observe as the associated electromagnetic emission will be faint by the time the shock reaches those distances.

deviation from spherical symmetry with a geometrical filling factor f , we revise the estimate of the CSM mass using two methods, leading to $M_{\text{CSM}} \sim 2.0(\sqrt{f}) M_{\odot}$ based on $\text{EM}(t)$ or $M_{\text{CSM}} \sim 1.2(f) M_{\odot}$ based on $\text{NH}_{\text{int}}(t)$. These analytical estimates are in broad quantitative agreement with the inferences by Vargas et al. (2022) from numerical modeling and simulations of SN 2014C.

The presence, mass, location, and chemical composition of the CSM are not consistent with traditional line-driven winds, and require the exploration of alternative models of time-dependent mass-loss mechanisms in evolved massive stars. In this paper we considered three models: WR-RSG wind–wind interaction, interaction with a binary companion, or a H-envelope ejection model triggered by nuclear burning instabilities or gravity waves. While the wind–wind interaction model has observational counterparts in our galaxy and does not require eruptive mass loss, the exceedingly short WR phase implied makes it highly unlikely. Current models of wave-driven mass loss or mass loss related to nuclear burning instabilities tend to predict small mass ejections at timescales very close to core collapse ($\lesssim \text{yr}$) that translate in CSM distances that are significantly smaller than in SN 2014C (Figure 13, lower panel). Additionally, for the small mass of the stellar progenitor of SN 2014C ($\sim 3.5\text{--}11 M_{\odot}$; Milisavljevic et al. 2015; Sun et al. 2020), instabilities would need to extend to the C-burning phase (Figure 13, upper and middle panels).

We conclude that mass loss associated with the interaction with a binary companion is the most likely explanation for the phenomenology of SN 2014C. However, the large dynamic range of CSM masses and timescales of the mass-loss episodes before explosion inferred for our large sample of SN interacters is likely a signature of a variety of mass-loss mechanisms at play. For example, while binary interaction may be able to account for the extremes of the distributions of CSM masses and timescales of the observed values, it does not offer a natural explanation for the extremely compact ($r \lesssim 10^{14}$ cm), thick CSM environments around some type IIP SNe (Figure 13, lower panel). For these cases of very compact CSM around the explosion site, mass-loss mechanisms related with the nuclear burning history of the primary star offer a more natural solution to the observed timing with core collapse.

Deep observations by sky surveys to look for pre-SN emission combined with rapid follow-up in the X-ray and radio band can reveal important information about the underlying mass-loss mechanisms within massive, evolved stars. Better constraints on CSM mass, location, and pre-explosion ejection time will subsequently provide an avenue to dispel uncertainty surrounding these crucial mass-loss mechanisms, such as which mechanisms dominate in particular stars, the timescales at which those mechanisms dominate, and the observational signatures of each mechanism.

We thank Cristiano Guidorzi, Brian Grefenstette, and Sayan Chakraborti for their contributions to the proposals that led to the data presented, without which this paper would not be possible.

We are extremely grateful to the efforts by the entire CXO and NuSTAR teams without which this unique data set would simply not exist.

This work made use of data from the NuSTAR mission, a project led by the California Institute of Technology, managed

by the Jet Propulsion Laboratory, and funded by the National Aeronautics and Space Administration. This research has made use of the NuSTAR Data Analysis Software (NuSTARDAS) jointly developed by the ASI Science Data Center (ASDC, Italy) and the California Institute of Technology (USA). This project is partially supported by NASA under contracts NNX17AI13G and NNX17AG80G. Support for this work was provided by the National Aeronautics and Space Administration through Chandra award Nos. GO6-17054A and GO9-20060A, issued by the Chandra X-ray Center, which is operated by the Smithsonian Astrophysical Observatory for and on behalf of the National Aeronautics Space Administration under contract NAS8-03060. This research has made use of data obtained from the Chandra Data Archive and the Chandra Source Catalog, and software provided by the Chandra X-ray Center (CXC) in the application packages CIAO and Sherpa.

D.B. acknowledges support from the NASA Illinois Space grant and the Northwestern Summer Undergraduate Research grant. R.M. acknowledges support by National Science Foundation under award Nos. AST-1909796 and AST-1944985. D.M. acknowledges NSF support from grants PHY-1914448 and AST-2037297. F.V. and F.D.C. acknowledge support from the UNAM-PAPIIT grant AG100820. L.D. is grateful for the partial financial support of the IDEAS Fellowship, a research traineeship program funded by the National Science Foundation under grant DGE-1450006. W.J.-G. is supported by the National Science Foundation Graduate Research Fellowship Program under grant No. DGE-1842165. W.J.-G. acknowledges support through NASA grants in support of Hubble Space Telescope program GO-16075 and 16500.

Facilities: NuSTAR, CXO.

Software: astropy (Astropy Collaboration et al. 2013), python, pyplot, CIAO v. 4.12 (Fruscione et al. 2006), NuSTARDAS v. 1.9.5, XSPEC (Arnaud 1996), CALDB (Graessle et al. 2006).

Appendix A

Inferences on the Environments of SNe in the Comparison Sample

Here we describe our methodology in collecting and estimating information on the mass loss of stars from their supernovae (SNe). We organize them chronologically and group them by the paper they were announced in.

A.1. SN 1987A

SN 1987A is a type II stellar explosion that has been monitored across the electromagnetic spectrum. Early theoretical modeling by Chevalier & Liang (1989) suggested that the CSM has an inner radius of 5×10^{17} cm, a thickness of 1.6×10^{15} cm, and contained $0.1 M_{\odot}$. Radio band observations by Cendes et al. (2018) have shown that after $\delta t \approx 9300$ days, the shock has broken out of the extended CSM ring based on the acceleration of the shock. Cendes et al. (2018) calculated a shock speed of $\sim 2300 \text{ km s}^{-1}$ within the CSM. The shock propagated through the CSM since $\delta t \approx 5500$, and therefore the CSM has an outer radius of $\sim 5.7 \times 10^{17}$ cm.

A.2. SNe 1987F, 1988Z, 1994W, 1994aj, 1995G, 1995N, 1996L, 1997ab, 1997eg, 1998S, 2005gl, 2005ip, 2006tf, and 2008iy

SNe of type IIn with mass-loss rates inferred from a combination of optical spectroscopy and light-curve modeling. We calculate the amount of mass between 10^{11} cm and 2×10^{16} cm to draw a direct comparison to SN 2014C by assuming a wind profile density with wind velocity and mass-loss rate from Table 9 of Kiewe et al. (2012). Onset of interaction is assumed to be 0 days because the earliest spectra of each SNe showed type IIn features. The lookback time for each SN was calculated by dividing the assumed 2×10^{16} cm by the wind velocity.

Original classification spectra are as follows: 1987F (Wegner & Swanson 1996), 1988Z (Heathcote et al. 1988), 1994W (Bragaglia et al. 1994), 1994aj (Benetti 1994), 1995G (Filippenko & Schlegel 1995), 1995N (Pollas et al. 1995), 1996L (McNaught et al. 1996), 1997ab (Hagen & Reimers 1997), 1997eg (Filippenko & Barth 1997), 1998S (Li et al. 1998), 2005gl (Blanc et al. 2005), 2005ip (Modjaz et al. 2005), 2006tf (Quimby et al. 2007), and 2008iy (Green 2009).

While we adopt the type IIn SN classification of Kiewe et al. (2012), we note that some of these classifications are contested. For example, Pastorello et al. (2018) pointed out odd properties such as missing nucleosynthesis elements that would be expected if SN 2005gl were a true SN as well as some similarities to SN 2009ip (see details below), and SN 2006tf could nearly be classified as an SLSN (Smith et al. 2008a).

A.3. SNe 1993J and 2011dh

SNe 1993J and 2011dh are type IIB SNe (Nomoto et al. 1993; Arcavi et al. 2011) that showed strong radio and X-ray emission (Fransson et al. 1996; Soderberg et al. 2012). Based on the modeling of these observations, Kundu et al. (2019) inferred a mass-loss rate of 4×10^{-5} and $4 \times 10^{-6} M_{\odot} \text{ yr}^{-1}$ for SNe 1993J and 2011dh, respectively, that lasted for the 6500 yr and 3000 yr prior to explosion assuming a 10 km s^{-1} wind velocity. We infer CSM masses of 0.26 and $0.012 M_{\odot}$, respectively, by multiplying the mass-loss rate by the number of years prior to explosion the mass loss began. Additionally, Kundu et al. (2019) assumed that the CSM of 1993J extends out to 2×10^{17} cm.

A.4. SN 1996al

SN 1996al is a type IIL stellar explosion (Benetti & Neuhauser 1996) that showed a remarkable evolution in its $H\alpha$ lines. The optical spectroscopy of SN 1996al showed a transition from early time ($\delta t \lesssim 140$ days) narrow lines to the appearance of a three-component line emission (Benetti et al. 2016). Benetti et al. (2016) interpreted this complex H line emission as being due to a two-component CSM: (i) an extended equatorial disk extending from an inner radius of 3×10^{15} to beyond 5×10^{17} cm (due to the latest spectrum at $\delta t \approx 5500$ days still showing signs of interaction) and (ii) a highly clumped CSM within 3×10^{15} cm. Benetti et al. (2016) estimated that the CSM mass contained within 3×10^{16} cm is $0.13 M_{\odot}$. Benetti et al. (2016) modeled the light curve and estimated a CSM speed of 1300 km s^{-1} , which would indicate the mass-loss event would have started ~ 120 yr prior to explosion.

A.5. SN 1996cr

SN 1996cr is a type IIn SN explosion (Bauer et al. 2008) that showed a late-time increase in radio and X-ray luminosity (Dwarkadas et al. 2010). Despite exploding in 1996, the first optical spectroscopic observations occurred 11 yr post-explosion, and so early time typing is unknown. Dwarkadas et al. (2010) estimated a dense CSM of density $\sim 8.2 \times 10^{-22} \text{ g cm}^{-3}$ from the progenitor that extends to 1.5×10^{17} cm. They predicted a mass-loss episode occurred within the 10^4 yr before stellar death and generated a $0.64 M_{\odot}$ CSM. Additionally, they calculated a lower-limit mass-loss rate of 1000 km s^{-1} winds to be $\sim 3.3 \times 10^{-9} M_{\odot} \text{ yr}^{-1}$ and an upper limit of $\sim 2 \times 10^{-5} M_{\odot} \text{ yr}^{-1}$.

A.6. SNe 1999cq, 2002ao, and 2006jc

SNe 1999cq, 2002ao, and 2006jc are type Ib SNe (Filippenko 1999; Gal-Yam et al. 2002; Crots et al. 2006) observed in the optical band photometrically and spectroscopically. They each interacted with an H-poor but He-rich environment. Foley et al. (2007) presented optical spectra of each, focusing on SN 2006jc, and showed spectra with evidence for interaction at 20, 27, and 19 days, respectively. Foley et al. (2007) measured a wind speed of 500 km s^{-1} for SN 2006jc and estimated that the CSM had been ejected ~ 2 yr prior to explosion. At an assumed ejecta velocity of $10,000 \text{ km s}^{-1}$, considering the SNe must have been interacting at the time of the spectra presented in Foley et al. (2007), the CSM must have resided within $\sim 2 \times 10^{15}$ cm for each SN.

A.7. SNe 1999em, 1999gi, 2001X, 2003Z, 2003hn, 2004et, 2005cs, 2009N, 2009ib, 2012A, 2012aw, 2012ec, 2013ab, 2013by, 2013ej, LSQ13dpa, 2014cy, ASASSN-14dq, ASASSN-14gm, and ASASSN-14ha

SNe of type-IIP/L with CSM mass, radial extension, and density parameter K inferred from a combination of optical and UV light-curve modeling (see Table 2 in Morozova et al. 2018). We calculate the mass-loss rate by assuming a wind-density profile and multiplying K by $4\pi v_w$, where v_w is their assumed wind speed (10 km s^{-1}). The onset time of interaction is assumed to the explosion time, as the UV excesses that are signatures of interaction are detected from the start of UV observations. Lookback time is calculated by dividing the radial extension by the wind speed.

Additionally, we note that SN 2005cs is considered a peculiar “subluminous” type IIP (Pastorello et al. 2006) while SN 2009N is considered an intermediate between “subluminous” and typical (Takáts et al. 2014).

A.8. SN 2001em

SN 2001em is a type Ib SN (Filippenko & Chornock 2001; Shivvers et al. 2019) that later evolved into a type IIn stellar explosion (Soderberg et al. 2004), and it was observed in the radio, X-ray, and optical (Chugai & Chevalier 2006; Chandra et al. 2020). Chugai & Chevalier (2006) estimated a $\sim 3 M_{\odot}$ CSM contained between ~ 6 and 7×10^{16} cm. They estimated that a mass-loss rate of $2\text{--}10 \times 10^{-3} M_{\odot} \text{ yr}^{-1}$ over the course of 1000–2000 yr prior to explosion could generate such a CSM.

A.9. SN 2003gk

SN 2003gk is a type Ib SN (Sollerman et al. 2003) observed in the radio with VLA (Bietenholz et al. 2014). We estimate the mass and mass-loss rate using the density parameter A as defined by Bietenholz et al. (2014). The mass-loss rate is defined as $A4\pi v_w$, and the density profile is defined as $\rho_{\text{CSM}}(R) = Ar^{-2}$ for a wind. We integrate this density profile out to 2.4×10^{17} cm, the location of the shockwave at 8 yr post-explosion. Using an assumed minimum and maximum wind velocity of 10 and 1000 km s⁻¹, we calculate a mass-loss rate of 10^{-7} – $10^{-5} M_{\odot} \text{ yr}^{-1}$ and a CSM mass of $7.6 \times 10^{-4} M_{\odot}$.

A.10. SN 2004C

SN 2004C is a type IIb SN observed at radio frequencies. DeMarchi et al. (2022) estimated an extended CSM at $\sim 5 \times 10^{15}$ to 10^{16} cm consisting of at least $0.021 M_{\odot}$ of density $1.5 \times 10^{-18} \text{ g cm}^{-3}$. They estimate that this corresponds to a mass-loss rate of at most $\sim 5 \times 10^{-3} M_{\odot} \text{ yr}^{-1}$. Assuming a wind speed of 1000 km s⁻¹, dividing the radius by the wind velocity gives that the mass-loss episode must have occurred approximately 6.5 yr prior to explosion.

A.11. SN 2004cc

SN 2004cc is a type Ic SN (Foley et al. 2004) observed in the radio band. Wellons et al. (2012) estimated that between 10 and 100 yr prior to explosion, the progenitor ejected between 10^{-4} and $10^{-3} M_{\odot}$ of material at a rate of $1.3 \times 10^{-4} M_{\odot} \text{ yr}^{-1}$, under an assumed 1000 km s⁻¹ wind velocity. While the outer radius of the shell is unconstrained, Wellons et al. (2012) calculated that the shell inner radius is between 2.6×10^{15} and 2.7×10^{16} cm.

A.12. SN 2004dk

SN 2004dk is a type Ib SN (Filippenko et al. 2004) that later showed H α emission from optical spectra and evolved into a type IIn (Mauerhan et al. 2018), and showed strong H α emission out to 13 yr post discovery. Mauerhan et al. (2018) estimate an inner CSM radius of $\sim 4 \times 10^{17}$ cm, corresponding to $\delta t = 1660$ days at an assumed 0.1c shock velocity, which was the beginning of radio re-brightening. As interaction is ongoing as of the latest spectra at $\delta t = 4684$ days, they place a lower limit on the outer radius to be 10^{18} cm. Additionally, Mauerhan et al. (2018) assumed a wind speed of 400 km s⁻¹ based on spectral feature measurements at late time, which would indicate the mass-loss episode occurred roughly 320 yr prior to explosion. They also specify that an increased wind speed of 1000 km s⁻¹ would instead correlate to approximately 125 yr prior to explosion. The mass-loss rate calculated from radio data indicates $6.3 \times 10^{-6} M_{\odot} \text{ yr}^{-1}$. Using these measurements, we assume a wind-density profile and estimate a CSM mass of $0.002 M_{\odot}$ by integrating the density over the inner and outer radii.

A.13. SN 2004gq

SN 2004gq is a type Ib SN (Filippenko & Foley 2004) observed in the radio. Wellons et al. (2012) estimated that between 10 and 100 yr prior to explosion, the progenitor ejected material at a rate of $\sim 9 \times 10^{-6} M_{\odot} \text{ yr}^{-1}$, under an assumed 1000 km s⁻¹ wind velocity. While the outer radius of

the shell is unconstrained, Wellons et al. (2012) calculated that the shell inner radius is between 6.2×10^{15} and 6.7×10^{15} cm.

A.14. SNe 2005kj, 2006aa, 2006bo, 2006jd, 2006qq, and 2008fq

These SNe are of spectroscopic type IIn; optical photometric and spectroscopic data were acquired for each object. Table 21 of Taddia et al. (2013) provides the wind speed, mass-loss rate, inner and outer radii of CSM, and the time before explosion. In the cases that both the mass-loss rate and time before explosion are estimated, we infer the mass of the CSM by multiplying their given values.

A.15. SN 2006Y, 2006ai, and 2016egz

These SNe are of spectroscopic type IIP (Green 2006; Fraser et al. 2016) with short-lived plateaus (approximately tens of days) partially powered by CSM interaction. Hiramatsu et al. (2021a) used optical/near-IR (NIR) light curves and spectroscopy to inform simulations and fit models to find best-fit parameters of the CSM. All simulations use an assumed RSG wind velocity of 10 km s⁻¹, and found that all three SNe experienced a wind-driven mass-loss rate of $0.01 M_{\odot} \text{ yr}^{-1}$. They found that SN 2006Y is best fit by a $0.01 M_{\odot}$ CSM, SN 2006ai with $0.03 M_{\odot}$, and SN 2016egz with $0.03 M_{\odot}$. From this, they estimated SN 2006Y experienced mass loss for 10 yr prior to explosion, while SN 2006ai and SN 2016egz for 30 yr prior to explosion. We calculate by multiplying the time frame of mass loss by the wind speed that the CSM extends to $\sim 3 \times 10^{14}$ cm for SN 2006Y and $\sim 9 \times 10^{14}$ cm for SN 2006ai and SN 2016egz.

A.16. SN 2006gy

SN 2006gy is a type IIn SLSN (Foley et al. 2006). Moriya et al. (2013) fit the light curve of SN 2006gy using a variety of models with varying density profiles, FS velocity, and CSM location. Moriya et al. (2013) reported that wind-like profiles fail to fit the light curve, while a much steeper profile, $\rho_{\text{CSM}} \propto R^{-5}$, and a constant density profile fit the light curve better. All results are reported in Table 1 of Moriya et al. (2013). The average mass-loss rate of all models is $0.1 M_{\odot} \text{ yr}^{-1}$, while the average CSM mass is $15 M_{\odot}$. The average inner radius of the CSM is $\sim 3 \times 10^{15}$ cm, and the average outer CSM radius is $\sim 1.6 \times 10^{16}$ cm. Using the assumed wind velocity of 100 km s⁻¹, the CSM would have been ejected ~ 50 yr prior to explosion.

A.17. SN 2007od

SN 2007od is a type IIP stellar explosion (Blondin & Calkins 2007) that showed atypically steep declines after the plateau phase ($\delta t \approx 100$ days) in brightness and “intermediate-width” (1500 km s⁻¹) H α features in optical photometry and spectroscopy (Andrews et al. 2010). Andrews et al. (2010) showed models that estimate the CSM inner radius to be between 700 and 1700 au (1 – 2.5×10^{16} cm) that had been ejected between 300 and 800 yr prior to explosion from a 1500 km s⁻¹ wind velocity. Additionally, Andrews et al. (2010) reported that the multi-peaked nature of the H α emission is consistent with a ring or torus-shaped CSM. No estimate of mass or mass-loss rate is given.

A.18. SN 2008es

SN 2008es is an SLSN type II (Yuan et al. 2008) that at early times showed no narrow features in its optical spectra. Bhirombhakdi et al. (2019) estimated from optical and infrared photometry that its CSM mass is between 2 and 3 M_{\odot} located between $\sim 2 \times 10^{14}$ to $\sim 2 \times 10^{15}$ cm. They also calculated that this would have required a mass-loss rate between 0.1 and 1 $M_{\odot} \text{ yr}^{-1}$ under their assumption of 100 km s^{-1} wind velocity. This additionally gives a lookback time of 0.5–1.6 yr prior to explosion. Bhirombhakdi et al. (2019) also reported that similar IR/optical measurements could be obtained by a magnetar spin-down model instead of a CSM-powered luminosity.

A.19. SN 2009ip Outburst A and B in 2012

SN 2009ip is a type IIn SN for which observations exist across the electromagnetic spectrum (radio, optical, X-rays, and gamma-rays; Margutti et al. 2014). Margutti et al. (2014) estimated that a dense CSM shell was located at $\sim 5 \times 10^{14}$ cm from the progenitor and extended to $\sim 4 \times 10^{16}$ cm.

A.20. SN 2009kf

SN 2009kf is a type IIP SN (Rodney et al. 2009) observed in the optical and UV bands. Through light-curve modeling, Moriya (2015) estimated that hydrogen-rich material extended to $\sim 10^{15}$ cm and was the result of mass-loss rate of 0.01 $M_{\odot} \text{ yr}^{-1}$ (under their assumption of 10 km s^{-1} winds). We estimate by dividing the radius by the wind velocity that the progenitor would have to be losing mass for approximately 32 yr prior to explosion, which would have produced $\sim 0.3 M_{\odot}$ of CSM.

A.21. SNe 2010al and 2011hw

SNe 2010al and 2011hw are both type Ibn SNe (Valenti et al. 2011; Pastorello et al. 2015a) that were monitored in the UV, IR, and optical bands, both spectroscopically and photometrically. Pastorello et al. (2015a) identified that SN 2010al required reclassification based on a $\delta t \approx 12$ days spectrum to Ibn, and that SN 2010al continued to show signs of interaction until the epoch of the last spectrum presented at $\delta t \approx 60$ days with a derived wind velocity of at least 1000 km s^{-1} . SN 2011hw, however, was not H-free, and Pastorello et al. (2015a) suggested it could be a transitional SN between Ibn and IIn, and present spectra from $\delta t \approx 1$ day to $\delta t \approx 72$ days with signs of interaction. These estimates, assuming a 10,000 km s^{-1} ejecta velocity, would place a constraint on the CSM inner radius within $\lesssim 6 \times 10^{14}$ and 8×10^{13} cm for SNe 2010al and 2011hw, respectively.

A.22. SN 2010jl

SN 2010jl is a particularly luminous type IIn SN (Benetti et al. 2010) that showed signs of an $\gtrsim 3 M_{\odot}$ CSM in the IR, optical, UV, and X-rays, resulting from an extensive period of $\gtrsim 0.1 M_{\odot} \text{ yr}^{-1}$ mass loss (Fransson et al. 2014). These estimates are lower limits due to uncertainties in the shock velocity. Fransson et al. (2014) inferred a wind velocity of $\sim 100 \text{ km s}^{-1}$ from the optical spectra, which they argued rules out an RSG progenitor. Strong interaction continues until the last optical spectra at ~ 1100 days, placing a lower limit of the CSM outer radius to be 2×10^{16} cm. Using the measured wind speed, this indicates the mass ejection had been occurring for at least ~ 60 yr prior to explosion. Fransson et al. (2014) also

discussed an IR light echo caused by dust at a distance of 6×10^{17} cm, which, if part of a previous mass ejection, would indicate a lookback time of ~ 1900 yr.

A.23. SN 2010mb

SN 2010mb is a type Ic stellar explosion (Ben-Ami et al. 2012) that interacted with hydrogen-poor material observed in the optical and could possibly be reclassified as a type Icn, with lines of width $\sim 800 \text{ km s}^{-1}$. Ben-Ami et al. (2014) observed SN 2010mb in the optical and UV bands, obtaining both photometric and spectroscopic data. From their modeling, they estimated a CSM mass of approximately 3.3 M_{\odot} , ejected 2.2 yr prior to explosion. We estimate the radius of the CSM shell by multiplying their ejecta velocity (5000 km s^{-1}) by the time until interaction onset (150 days) to get $\sim 6.5 \times 10^{15}$ cm. Similarly, we estimate the outer radius by using the time at which interaction ceases (750 days). Ben-Ami et al. (2014) measured the wind speed to be 800 km s^{-1} , which we then use to calculate the mass-loss rate of $\sim 0.25 M_{\odot} \text{ yr}^{-1}$ by setting the CSM mass equal to the integral of the wind-density profile and integrating over the shell.

A.24. SN 2010mc

SN 2010mc is a type IIn SN (Howell & Murray 2012) for which an outburst was observed 40 days prior to explosion. Ofek et al. (2013) used optical spectra to model the surrounding CSM. They estimated the CSM was located between 7×10^{14} cm and 10^{16} cm and contained 0.01 M_{\odot} .

A.25. PTF10aagc

PTF10aagc is an SLSN that was originally a type I but later showed signs of strong $\text{H}\alpha$ emission (Yan et al. 2015). Yan et al. (2015) derived constraints on the surrounding CSM that caused the transition using optical spectroscopy and photometry and found that based on the width of the narrow $\text{H}\alpha$, the CSM had a velocity between 230 and 400 km s^{-1} . Additionally, Yan et al. (2015) estimated an ejecta velocity of 13,000 km s^{-1} . Because the $\text{H}\alpha$ emission appeared in a $\delta t \approx 322$ days, Yan et al. (2015) estimated a CSM radius of $\sim 4 \times 10^{16}$ cm and assumed a CSM shell width of 10%. In order to travel that distance at 230–400 km s^{-1} , Yan et al. (2015) calculated the ejection must have occurred at least 40 yr prior to explosion. Yan et al. (2015) also reported that due to a lack of absorption, they can place an upper limit of the CSM mass to be $\lesssim 30 M_{\odot}$.

A.26. SN 2011fh

SN 2011fh is a type IIn SN (Monard et al. 2011a) that showed a high degree of similarity to SN 2009ip both spectroscopically and photometrically (Pessi et al. 2022), displaying multiple eruptive phases in the years following the initial “explosion” in 2011 in the NIR and optical. Prominent $\text{H}\alpha$ lines remain strong from the first spectrum at 3 days post-explosion out to 1359 days post-explosion. Pessi et al. (2022) assumed a CSM velocity of 100 km s^{-1} , which gives a mass-loss rate of $4 \times 10^{-2} M_{\odot} \text{ yr}^{-1}$.

A.27. SN 2011ht

SN 2011ht is a type IIn SN (Prieto et al. 2011), modeled by Roming et al. (2012) using optical and UV photometry and

spectroscopy. They calculated that the CSM resides between 5×10^{14} and 10^{15} cm and contains between 0.01 and $1 M_{\odot}$. Using their assumed wind velocity of 600 km s^{-1} , they stated that this implies a mass-loss rate of $3\text{--}5 \times 10^{-4} M_{\odot} \text{ yr}^{-1}$ and the mass loss occurred ~ 1 yr prior to explosion.

A.28. SN 2011ja

SN 2011ja is a type IIP SN (Monard et al. 2011b) that showed late ($\sim 60\text{--}80$ days post-explosion) signs of $H\alpha$ and $H\beta$ in optical spectra. Andrews et al. (2016) interpreted this as interaction with a disk-like CSM tilted at a 45° angle from the viewing direction. Andrews et al. (2016) estimated a mass-loss rate of $0.02\text{--}1 \times 10^{-5} M_{\odot} \text{ yr}^{-1}$ for their measured wind velocity of 180 km s^{-1} and an inner CSM radius of $\sim(4\text{--}50) \times 10^{15}$ cm. Given the wind velocity, we infer a lookback time of $\sim 8\text{--}14$ yr prior to explosion, which in turn combined with the mass-loss rate would give a CSM mass of $\sim 0.01\text{--}1 \times 10^{-4} M_{\odot}$.

A.29. iPTF11iqb

iPTF11iqb is a type IIIn SN that later evolved into a type III/LP that showed evidence for a two-component medium (Smith et al. 2015). Smith et al. (2015) suggested a CSM shaped by two different mass-loss rates: a mass-loss rate of $0.4 \times 10^{-5} M_{\odot} \text{ yr}^{-1}$ for $(0.1\text{--}3) \times 10^{15}$ cm, and a mass-loss rate of $1.5 \times 10^{-5} M_{\odot} \text{ yr}^{-1}$ at $(3\text{--}300) \times 10^{15}$ cm. These distances correspond to upper limits of 8 yr and 1000 yr prior to explosion, respectively, using their assumption of 100 km s^{-1} winds. Finally, Smith et al. (2015) calculated a 0.001 and $0.04 M_{\odot}$ CSM mass for the inner and outer components, respectively.

A.30. PTF11qcj

PTF11qcj is a type Ic SN (Corsi et al. 2012) with radio, IR, and optical light-curve coverage in addition to optical spectroscopy (Corsi et al. 2014). Corsi et al. (2014) calculated that the CSM inner radius is $\sim 10^{16}$ cm. They estimated the CSM had been ejected at a speed of 1000 km s^{-1} with a mass-loss rate of $\sim 10^{-4} M_{\odot} \text{ yr}^{-1}$, approximately 2.5 yr prior to explosion. While they do not estimate the outer radius, they do give a lower limit of $\sim 2 \times 10^{17}$ cm.

A.31. OGLE-2012-SN-006

OGLE-2012-SN-006 is a type Ibn SN observed in the IR and optical bands both spectroscopically and photometrically (Pastorello et al. 2015b). Pastorello et al. (2015b) showed the light curve was significantly shallower than that expected of typical radioactive $^{56}\text{Co}\text{--}^{56}\text{Fe}$ decay starting at 25 days post-explosion and spectra showed signatures of H-poor interaction through ~ 190 days, and measured a wind speed of 250 km s^{-1} . Assuming an ejecta velocity of $10,000 \text{ km s}^{-1}$, this would imply an inner CSM radius of at least $\sim 5 \times 10^{13}$ cm.

A.32. SN 2012aa

SN 2012aa is a highly luminous type Ic SN (Cenko et al. 2012) that was shown to experience interaction with hydrogen-free material (Roy et al. 2016). While SN 2012aa did not reach the luminosity of a typical SLSN, it still reached magnitude -20 in the optical band, placing it at an intermediate luminosity between typical SN type Ic and SLSN. SN

2012aa went on to show a second bump in its optical light curve, which Roy et al. (2016) explained as interaction with a dense CSM. They show that interaction begins approximately 65 days post-explosion and ends 95 days post-explosion. Using their assumed ejecta velocity of 10^4 km s^{-1} , this translates to a shell located between ~ 5 and 8×10^{16} cm. They estimated the CSM contains between 5 and $10 M_{\odot}$, which we use to estimate a mass-loss rate between ~ 0.006 and $0.01 M_{\odot} \text{ yr}^{-1}$ using their assumed wind velocity of 1000 km s^{-1} . Similarly, we also use the same assumed wind velocity to estimate the lookback time as the radius divided by the velocity to get $\sim 2\text{--}3$ yr prior to explosion.

A.33. SN 2013L

SN 2013L is a type IIIn SN (Monard et al. 2013) that showed prominent hydrogen spectral features and was observed across the UV, optical, and IR (Taddia et al. 2020). Taddia et al. (2020) estimated an enhanced mass-loss rate of $0.017\text{--}0.15 M_{\odot} \text{ yr}^{-1}$ in the $25\text{--}40$ yr prior to explosion. Additionally, they calculated that this corresponds to a mass of $3.8\text{--}6.3 M_{\odot}$ with a measured wind velocity of $120\text{--}240 \text{ km s}^{-1}$ extending from the progenitor surface to $\sim 0.9\text{--}3 \times 10^{16}$ cm.

A.34. SN 2013cu

SN 2013cu is a type IIb (Gal-Yam et al. 2014) that was discovered very early and was rapidly classified 15.5 hr post-explosion. The SN already showed signs of interaction with a wind ($v_w \sim 100 \text{ km s}^{-1}$) that was rich in both H and He (Groh 2014). Groh (2014) fit the optical spectrum and estimated a mass-loss rate of $3 \times 10^{-3} M_{\odot} \text{ yr}^{-1}$. Their modeling also estimated the CSM inner radius $R_{\text{in}} = 1.5 \times 10^{14}$ cm and extending to 2×10^{15} cm, for a total mass of $0.022 M_{\odot}$. Using the wind speed from Groh (2014) and their modeled radius, this would indicate a mass-loss period ranging from $\sim 6\text{--}60$ yr prior to explosion. Groh (2014) predicted that these properties could be the result of a yellow hypergiant or LBV star progenitor.

A.35. SN 2013df

SN 2013df is a type IIb SN (Ciabattari et al. 2013), showing signs of interaction in its spectrum within the first 10 days. Kamble et al. (2016) observed SN 2013df in the radio and X-rays and estimated a mass-loss rate of $\sim 0.7\text{--}1.4 \times 10^{-4} M_{\odot} \text{ yr}^{-1}$ for an assumed wind velocity of 10 km s^{-1} .

A.36. PS1-13arp

PS1-13arp is a type IIP SN (Gezari et al. 2015) with an early UV excess of emission in addition to its optical light curve (Gezari et al. 2015; Haynie & Piro 2021). Haynie & Piro (2021) modeled the light curve in the context of a shock breaking through a dense CSM located at $\sim 1.3 \times 10^{14}$ cm and containing $0.08 M_{\odot}$. Using that radius and their assumed wind speed of 10 km s^{-1} , this would require the material to have been ejected approximately 4 yr prior to the explosion.

A.37. LSQ13ddu

LSQ13ddu is a type Ibn SN (Smartt et al. 2015) that exhibited a very short interaction phase that produced prominent helium lines in the optical spectra. The phase of strong interaction started sometime between explosion and the first spectrum at 5 days and ended between 6 and 11 days post-

explosion (Clark et al. 2020). Using the ejecta velocity from Clark et al. (2020) of $34,600 \text{ km s}^{-1}$ and the constraints on interaction times, this would place the CSM between ~ 1.5 and $3 \times 10^{15} \text{ cm}$. Additionally, Clark et al. (2020) estimated the mass of the CSM to be $0.59 M_{\odot}$.

A.38. SN 2013fs

SN 2013fs is a type IIP SN (Yaron et al. 2017) that showed signs of interaction within hours of discovery. Yaron et al. (2017) modeled the optical light curve and presented optical spectra to show that the flash ionization spectra observed was likely due to a dense CSM extending from ~ 1.2 to $10 \times 10^{14} \text{ cm}$. Their models derive a CSM wind speed between 15 and 100 km s^{-1} , which indicate the mass-loss was occurring on a timescale of $\sim 1 \text{ yr}$ prior to explosion. By calculating the time it would have taken for the CSM to reach the edge of the maximum distance of 10^{15} cm , we find the progenitor star would have been shedding mass for ~ 3 – 20 yr prior up until explosion. Considering the estimated mass-loss rate from Yaron et al. (2017) of 0.3 to $4 \times 10^{-3} M_{\odot} \text{ yr}^{-1}$, this would translate to a CSM mass between $\sim 9 \times 10^{-4}$ and $8 \times 10^{-2} M_{\odot}$.

A.39. iPTF13ehe, iPTF15esb, and iPTF16bad

SLSNe of type I that later showed $H\alpha$ emission in their optical spectra (Yan et al. 2017). Yan et al. (2017) estimated their CSMs began between ~ 4 and $9 \times 10^{16} \text{ cm}$ and contain between 0.05 and $3 M_{\odot}$. We estimate the lookback time by dividing the radius by assumed wind velocities of 100 and 1000 km s^{-1} to give ~ 1 – 30 yr prior to explosion.

A.40. SN 2014av

SN 2014av is a type Ibn SN (Pastorello et al. 2016) observed in the optical photometrically and spectroscopically. Pastorello et al. (2016) found that the spectrum taken at $\delta t \approx 18$ days post-explosion show features of a Ibn, while the spectra at $\delta t \approx 10$ days is largely featureless. Assuming an ejecta velocity of $10,000 \text{ km s}^{-1}$, this would place a CSM radius between 9 and $20 \times 10^{14} \text{ cm}$.

A.41. LSQ14efd, iPTF15dtg, and 2020bvc

LSQ14efd, iPTF15dtg, and 2020bvc are type Ic SNe that interacted with hydrogen-poor material. Jin et al. (2021) used optical light curves to inform simulations and constrain parameters of possible CSM that could result in the observed light curves. Their simulations produced 0.1 – $0.2 M_{\odot}$ of hydrogen-poor material beginning at either 10^{13} or 10^{14} cm , which had been ejected ~ 2.4 months prior to explosion. Based on their assumed wind velocity of 200 km s^{-1} , they report this would correspond to a mass-loss rate of 0.6 – $13 M_{\odot} \text{ yr}^{-1}$.

A.42. ASASSN-14ms

ASASSN-14ms is a highly luminous type Ibn (Holoien et al. 2017) that began interacting by the time of the first optical spectrum (which was acquired at 7 days) and continued through the last spectrum at 44 days post-explosion (Vallely et al. 2018). Vallely et al. (2018) modeled the optical photometry and extracted a CSM mass of $0.51 M_{\odot}$.

A.43. iPTF14hls

iPTF14hls is a type IIP SN (Li et al. 2015) that showed extremely long-lasting optical emission and photometric variability (Arcavi et al. 2017). A potential interpretation of this phenomenology is the SN shock interaction with a complex medium. Within this scenario, Arcavi et al. (2017) estimated the CSM contains tens of solar masses due to an ejection a few years prior to explosion.

A.44. SN 2015da

SN 2015 da is a type IIn SN (Tartaglia 2019) that was observed to have IR echoes due to a surrounding CSM shell (Tartaglia et al. 2020). Tartaglia et al. (2020) estimated, using optical light-curve modeling and spectra, the shell contains between ~ 5 and $10 M_{\odot}$ due to an enhanced mass-loss rate of 0.6 – $0.7 M_{\odot} \text{ yr}^{-1}$.

A.45. ASASSN-15no

ASASSN-15no is a type Ic SN (Balam & Graham 2015), but later spectra from Benetti et al. (2018) revealed the development of broad H lines in optical spectra, which led to a reclassification as type II SN. Combined with optical photometric data, Benetti et al. (2018) interpreted its spectral evolution and photometric data as evidence for a two-component structured CSM, composed of two shells: an H-rich CSM inner shell and an H-poor outer shell. Benetti et al. (2018) estimated the inner CSM to be a shell at $\sim 2 \times 10^{14} \text{ cm}$ of 1 – $2 M_{\odot}$ while the outer H-poor shell has an inner radius $\sim 3 \times 10^{15} \text{ cm}$ and extends to $\sim 8 \times 10^{15} \text{ cm}$. Using an assumed wind velocity of 10 – 100 km s^{-1} , Benetti et al. (2018) calculated lookback times of 0.7 – 7 and 9 – 90 yr for the inner and outer CSM, respectively.

A.46. iPTF16eh

iPTF16eh is a type I SLSN based on UV observations and optical spectroscopy (Lunnan et al. 2018). Lunnan et al. (2018) modeled the CSM structure based on simulations and estimated the dense hydrogen-poor shell has inner radius of $\sim 3 \times 10^{17} \text{ cm}$ that extends to $\sim 3.5 \times 10^{17} \text{ cm}$ and was ejected $\sim 32 \text{ yr}$ prior to explosion. They calculated that the shell contains 1 – $10 M_{\odot}$ with a measured wind speed of 3300 km s^{-1} .

A.47. SN 2016aps

SN 2016aps is a type IIn SLSN (Chornock et al. 2016) with optical photometry and spectroscopy data. The extreme energy output by this SLSN is thought to be the result of massive ejecta colliding with an extremely massive CSM. There are two separate models seeking to fit the optical light curve from Nicholl et al. (2020) and Suzuki et al. (2021), who estimated a CSM mass of $\sim 150 M_{\odot}$ (minimum of $40 M_{\odot}$) and $8 M_{\odot}$, respectively. Suzuki et al. (2021), using a radiation hydrodynamics simulation code designed for SLSNe, found that an outer CSM radius of 10^{16} cm best fits the data. This would indicate that for a wind range of 10 – 1000 km s^{-1} , the beginning of mass loss would have to be between ~ 3 and 300 yr prior to explosion. We emphasize the calculations from Suzuki et al. (2021) due to the use of specific numerical models.

A.48. *SN 2016iet*

SN 2016iet shows two optical peaks separated by approximately 100 days (Gomez et al. 2019). Gomez et al. (2019) estimated, based on optical light-curve modeling and spectroscopy, that the CSM was extremely massive at $\sim 38 M_{\odot}$ located between $1 - 7 \times 10^{14}$ cm, which corresponds to a mass-loss rate of $7 M_{\odot} \text{ yr}^{-1}$ assuming a 100 km s^{-1} velocity. They calculated that this would require ejection between 2 and 7 yr prior to explosion, but also noted that if the assumed velocity is increased to 1000 km s^{-1} this would place ejection within 70–260 days prior to explosion.

A.49. *AT 2016jbu*

AT 2016jbu is thought to be an SN-impostor event akin to 2009ip before 2012 (Bose et al. 2017), which appeared spectroscopically similar to a type IIn SN. In two papers, Brennan et al. (2022a) and Brennan et al. (2022b) proposed that the event likely occurred as a result of a highly asymmetric outburst of $0.05\text{--}0.14 M_{\odot} \text{ yr}^{-1}$ with an assumed wind velocity of 250 and 750 km s^{-1} based on the overall luminosity and narrow $\text{H}\alpha$ lines.

A.50. *SN 2017ahn*

SN 2017ahn is a type II SN (Hosseinzadeh et al. 2017) that displayed signs of interaction in its spectra within 6 days of explosion. Tartaglia et al. (2021a) used the spectra and optical light-curve modeling to predict a mass-loss rate of $2.7\text{--}4 \times 10^{-3} M_{\odot}$ that generated a CSM of inner radius $\sim 2 \times 10^{13}$ cm. Using the assumed wind speed from Tartaglia et al. (2021a) of 150 km s^{-1} , we infer a lookback time of ~ 18 days.

A.51. *SN 2017dio*

SN 2017dio is a type Ic SN (Cartier et al. 2017) that later evolved into a type IIn, showing narrow H and He lines in its optical spectra (Kuncarayakti et al. 2018). Kuncarayakti et al. (2018) estimated a mass-loss rate of $\sim 0.02 M_{\odot} \text{ yr}^{-1}$ that peaked in the few decades prior to explosion. They estimated a 10^4 km s^{-1} ejecta speed, which, based on the lack of narrow features in the $\delta t = 6$ days spectrum and the presence of narrow features, indicates the shockwave would have traveled between ~ 0.5 and 1×10^{15} cm before encountering the CSM. While there is no estimate for the outer radius, we can at least place a lower limit, as the last spectra taken presented was 83 days post-explosion, corresponding to at least $\sim 7 \times 10^{15}$ cm. The CSM has a measured speed of 500 km s^{-1} , which, integrating over a wind-density profile from the inner radius to the lower limit, produces a minimum CSM mass of $\sim 0.089 M_{\odot}$.

A.52. *SN 2017eaw*

SN 2017eaw is a type IIP (Xiang et al. 2017) that showed extensive signs of interaction at 900 days post-explosion from a transition of a narrow $\text{H}\alpha$ feature to a box-shaped $\text{H}\alpha$ feature (Weil et al. 2020). Weil et al. (2020) calculated from optical spectroscopy and light-curve modeling that 2017eaw had a mass-loss rate of $3 \times 10^{-6} M_{\odot} \text{ yr}^{-1}$ at least 1700 yr prior to explosion. They also estimated the CSM shell begins at $\sim 5.3 \times 10^{16}$ cm from their assumed 10 km s^{-1} wind velocity of red supergiants. While additional observations have not been taken to determine the extent of the CSM, if we assume the

shell extends to a similar distance as SN 2014C ($\sim 10^{17}$ cm), we estimate a mass of approximately $0.004 M_{\odot}$.

A.53. *SN 2017ens*

SN 2017ens is a superluminous type Ic-BL that later evolved into a type IIn (Chen et al. 2018) as revealed by optical and UV observations in addition to spectroscopy (Chen et al. 2018). Chen et al. (2018) estimated that the explosion interacted with a dense shell located between $\sim 10^{15}$ and 7×10^{16} cm. They were also able to measure a wind velocity of between 50 and 60 km s^{-1} and therefore calculate that the mass-loss rate was $\sim 5 \times 10^{-4} M_{\odot} \text{ yr}^{-1}$. Assuming a wind-density profile, we estimate the amount of mass contained within the shell by integrating the wind-density profile over the extent of the shell to get $\sim 0.06 M_{\odot}$. Additionally, we estimate the lookback time by dividing the radius by the wind speed to get a lookback time of ~ 7 yr.

A.54. *SN 2017gmr*

SN 2017gmr is a type IIP (Elias-Rosa 2017) that did not show narrow H features in optical spectra at early times (~ 2 days post-explosion), but did have a bump in the U and B filters that Andrews et al. (2019) suggested to be asymmetric CSM interaction. Interaction began at least 2 days post-explosion and is ongoing as of the last spectrum presented in Andrews et al. (2019) at 180 days post-explosion. From the combined UV, optical, and IR light curve, Andrews et al. (2019) estimated a progenitor radius (and therefore lower limit on the CSM radius) of $\sim 3 \times 10^{13}$ cm that extends to an outer radius of 1.8×10^{14} cm. From this radius and a measured wind velocity of 55 km s^{-1} , Andrews et al. (2019) predicted a lookback time of “years to decades.”

A.55. *SN 2017hcc*

SN 2017hcc is a type IIn SLSN (Prieto et al. 2017) for which a highly asymmetric CSM structure was invoked in order to explain the irregular H emission and absorption features (Smith & Andrews 2020). Smith & Andrews (2020) measured a 50 km s^{-1} wind velocity, and an $\text{H}\alpha$ component out to at least 848 days post-explosion. Using the measured broad-line $\text{H}\alpha$ emission that Smith & Andrews (2020) associated to the ejecta of 6000 km s^{-1} , that would place a lower limit on the outer radius of 4.4×10^{16} cm. Smith & Andrews (2020) estimated that the enhanced mass-loss episode was occurring for 6–12 yr prior to explosion at a rate of $1.4 M_{\odot} \text{ yr}^{-1}$, translating to 8–16 M_{\odot} of CSM.

A.56. *SN 2018zd*

SN 2018zd is a type IIP SN that shows hydrogen lines at 4.9 days post-explosion and eventually developed a plateau in its optical light curve and spectra (Hiramatsu et al. 2021b). Hiramatsu et al. (2021b) estimated that approximately 10 yr prior to explosion, SN 2018zd ejected $0.1 M_{\odot}$, at a rate of $0.01 M_{\odot} \text{ yr}^{-1}$. Using their assumed wind velocity of 20 km s^{-1} , we calculate that the shell would extend to $\sim 6 \times 10^{14}$ cm by multiplying the lookback time by the wind velocity.

A.57. *SN 2018gep*

SN 2018gep is a Ic-BL stellar explosion (Costantin et al. 2018) with an exceptionally short rise time of 0.5–3 days

(Ho et al. 2019), placing it among the fast blue optical transients. Leung et al. (2021a) estimated this was due to a $\sim 0.3 M_{\odot}$ CSM approximately beginning $\sim 0.7\text{--}1.5 \times 10^{15}$ cm from the progenitor based on simulations of the optical light curve.

A.58. SN 2018gix

SN 2018gix went through three distinct phases: (I) a hot blue spectrum with signatures of ionized CSM, (II) signatures of a type IIb, then (III) interaction with a helium-rich CSM that led to the classification as a type Ibn SN (Prentice et al. 2020). Prentice et al. (2020) calculated that the CSM is composed of $0.004\text{--}0.014 M_{\odot}$ of material located in a thin shell between $\sim 3.8 \times 10^{14}$ and $\sim 4.5 \times 10^{14}$ cm. They assumed a wind speed between 150 and 500 km s^{-1} , which we use to estimate a lookback time by dividing the radius by the wind velocity to get $\sim 0.2\text{--}0.8$ yr prior to explosion. Similarly, using the assumed wind velocity, Prentice et al. (2020) calculated a mass-loss rate of $(5\text{--}510) \times 10^{-4} M_{\odot} \text{ yr}^{-1}$.

A.59. SN 2018ijp

SN 2018ijp is a type Ic-BL stellar explosion (Fremming et al. 2018) that was discovered by Zwicky Transient Facility. Follow-up data include optical photometry and spectroscopy (Tartaglia et al. 2021b). Modeling these data, Tartaglia et al. (2021b) estimated a dense CSM located between $\sim 4.6 \times 10^{15}$ and 5×10^{16} cm. The CSM contains $0.5 M_{\odot}$ and corresponds to a mass-loss rate of $0.2 M_{\odot} \text{ yr}^{-1}$ originating $10\text{--}100$ yr prior to explosion.

A.60. SNe 2019jc and 2021ckj

SNe 2019jc and 2021ckj are both type Icn stellar explosions (Pellegrino et al. 2022) with optical photometry and spectroscopy. Pellegrino et al. (2022) modeled the light curve of SN 2019jc as being powered by shock interaction with a wind-density profile ($\rho_{\text{CSM}}(R) \propto R^{-2}$), and found the CSM contains $0.58 M_{\odot}$ of H- and He-poor material at an inner radius of $\sim 4.04 \times 10^{14}$ cm. Pellegrino et al. (2022) also measured a wind speed between 500 and 1000 km s^{-1} , which would imply a lookback time of ~ 26 days. SN 2021ckj has sparser data: Pellegrino et al. (2022) presented a spectrum at ~ 13 days with evidence for interaction. Assuming a minimum ejecta speed of 7000 km s^{-1} (as for SN 2019jc; Pellegrino et al. 2022), this ejecta speed implies a rough CSM distance of $\sim 7.7 \times 10^{14}$ cm.

A.61. SN 2019uo

SN 2019uo is a type Ibn SN (Fremming et al. 2019), for which the CSM properties were inferred by Strotjohann et al. (2021) through optical light-curve modeling. SN 2019uo was observed to have an outburst 320 days prior to explosion, which ejected at most $0.8 M_{\odot}$. It is unknown how far the CSM extends, but Strotjohann et al. (2021) estimated the inner shell radius to be between 3×10^{15} and 10^{16} cm, with a measured wind velocity of 880 km s^{-1} .

A.62. SN 2019cad

SN 2019cad is a type Ic stellar explosion (Burke et al. 2019) that had a second peak in its optical light curve approximately $45\text{--}60$ days post-explosion and showed prominent C and Si lines in its spectra (Gutiérrez et al. 2021). Using the ejecta

velocity derived in Gutiérrez et al. (2021) of $14,000 \text{ km s}^{-1}$ and the time and duration of the second peak, we infer that a CSM shell could exist between $\sim 2\text{--}6 \times 10^{15}$ cm.

A.63. SN 2019ehk

SN 2019ehk is a calcium-rich transient (Hung et al. 2019) that showed signs of shock interaction with an H-rich CSM in its optical spectra ~ 1.5 days post-explosion. The CSM mass inferred from optical and X-ray observations is $\sim 0.007 M_{\odot}$ for a wind velocity of $\sim 500 \text{ km s}^{-1}$ (Jacobson-Galán et al. 2020). The spectral features associated with shock interaction vanished by $\delta t \approx 2.4$ days, indicating an end to interaction with the dense CSM (Jacobson-Galán et al. 2020). This phase experienced a mass-loss rate of $\sim 0.01 M_{\odot} \text{ yr}^{-1}$ for ~ 0.6 yr prior to explosion, using the 500 km s^{-1} wind velocity from Jacobson-Galán et al. (2020). Additionally, Jacobson-Galán et al. (2020) estimated an upper limit for the mass-loss rate of $10^{-5} M_{\odot} \text{ yr}^{-1}$ beyond the thick CSM shell at $10^{16}\text{--}10^{17}$ cm based on radio observations. Since the nature of SN 2019ehk as a core-collapse event is disputed, and a connection with white-dwarf explosions is not excluded, we leave SN 2019ehk out of Figures 11, 12, and 13. Similarly, we leave SN 2021gno, another calcium-rich SN (Jacobson-Galán et al. 2022a) with detected X-ray emission out of the sample.

A.64. SN 2019hgp

SN 2019hgp is a type Icn SN (Gal-Yam 2021) that within a day of explosion began interacting with a 1900 km s^{-1} wind rich in C and O (Gal-Yam et al. 2022). Gal-Yam et al. (2022) estimated a CSM mass of $0.2 M_{\odot}$ CSM, resulting from a mass-loss rate of $0.004 M_{\odot} \text{ yr}^{-1}$. Using their modeled wind speed and the onset of interaction of ~ 1 day and the end of interaction at ~ 6 days as shown by spectra in Gal-Yam et al. (2022), this would place the CSM between $\sim 10^{13}$ and 10^{14} cm. Again using the 1900 km s^{-1} wind speed, this would correlate to a mass-loss episode within a month before explosion.

A.65. SN 2019oys

SN 2019oys is a type Ib SN that transitioned to a type IIn, much like SN 2014C (Fremming & Dahiwalé 2019; Sollerman et al. 2020). This transition occurred ~ 100 days post-explosion, and spectra still showed broad and strong H α to at least 200 days post-explosion.

A.66. SN 2019yvr

SN 2019yvr is a type Ib (Dimitriadis et al. 2019), but it later interacted with an H-rich CSM. Kilpatrick et al. (2021) found that the optical photometry and spectroscopic data are best fit by a two-part ejection model, one that occurred $50\text{--}100$ yr prior to explosion and removed most of the H-envelope, followed by a minor outburst within the last 2.6 yr that removed the remainder of the H-envelope. Using stellar models combined with spectroscopy, Kilpatrick et al. (2021) estimated that the final eruption removed a $0.01\text{--}0.03 M_{\odot}$ H-envelope from the star. The previous outburst does not have an estimated mass, but Kilpatrick et al. (2021) calculated a mass-loss rate of $1.3 \times 10^{-4} M_{\odot} \text{ yr}^{-1}$ for an assumed wind speed of 100 km s^{-1} . Based on the onset time of interaction, Kilpatrick et al. (2021) also estimated an inner CSM radius of ~ 1000 au, or $\sim 1.5 \times 10^{15}$ cm.

A.67. SN 2020oi

SN 2020oi is a type Ic SN (Siebert et al. 2020) that showed deviations from steady-state wind mass loss in the radio. SN 2020oi has been observed extensively in the optical and the UV by Maeda et al. (2021) and Gagliano et al. (2022). Maeda et al. (2021) estimated that the CSM has strong fluctuations compared to the expected power-law distribution within 10^{15} cm with a mass-loss rate of $\sim 0.3\text{--}1 \times 10^{-3} M_{\odot} \text{ yr}^{-1}$ and then returns to a smooth power law beyond 10^{16} cm. According to Maeda et al. (2021), this places the erratic mass loss within 1 yr of explosion based on the assumption of 1000 km s^{-1} velocities. We in turn thus infer a CSM mass of at most $0.001 M_{\odot}$.

A.68. SN 2020faa

SN 2020faa is a type II SN (Perley et al. 2020) for which optical photometry and spectroscopy has been acquired. $\text{H}\alpha$ appeared in its spectrum 12 days post-explosion, but was absent at least 6 days post-explosion (Yang et al. 2021). Based on calculations from Yang et al. (2021) of the blackbody radius at early times, we estimate that the CSM inner radius is $\sim 10^{15}$ cm.

A.69. SN 2020pni

SN 2020pni is a type II SN (Bruch et al. 2020). Modeling of optical-UV photometry and optical spectroscopy by Terreran et al. (2022) led to the inference of a CSM shell extending to $\sim 1.3 \times 10^{15}$ cm and containing between 0.04 and $0.12 M_{\odot}$. Terreran et al. (2022) assumed a wind velocity of 200 km s^{-1} ,

which corresponds to a mass-loss rate of $0.02\text{--}0.08 M_{\odot} \text{ yr}^{-1}$ for approximately 2 yr prior to explosion.

A.70. SN 2020tlf

SN 2020tlf is a type IIP/L stellar explosion (Balcon 2020) with detected pre-explosion eruptions, as well as early spectroscopic signatures of shock interaction and luminous UV emission (Jacobson-Galán et al. 2022b). By modeling these observations Jacobson-Galán et al. (2022b) inferred the presence of dense CSM with an extent to 10^{15} cm produced by a mass-loss rate of $\sim 10^{-2} M_{\odot} \text{ yr}^{-1}$ for an assumed wind speed of 50 km s^{-1} . Chugai & Utrobin (2022) provided further constraints, estimating a CSM mass of $0.2 M_{\odot}$ that had been ejected within 6 yr prior to explosion.

A.71. SN 2021csp

SN 2021csp is a type Icn explosion (Perley 2021) that showed prominent CIII lines of velocity 1800 km s^{-1} (Fraser et al. 2021). Fraser et al. (2021) estimated the CSM to extend to $\sim 400 R_{\odot}$ (2×10^{13} cm) and contain $\sim 1 M_{\odot}$ of H- and He-poor material. We infer from the wind velocity that this material was ejected only ~ 2 days prior to explosion.

Appendix B

Tables

Data tables for the CXO observations, NuSTAR observations, and their best-fitting parameters in Tables 2, 3, 4, 5, and 6.

Table 2
Chandra X-Ray Observations of SN 2014C

Chandra ID	Date (MJD)	Date (UT)	Exposure (ks)	Phase (days)	Count-rate 0.5–8 keV (c s^{-1})	Source Significance σ
16005	56964.33	11/3/14	12.4	308.33	$1.1 (\pm 0.09) \times 10^{-2}$	46.4
17569	57052.69	1/30/15	13.3	396.69	$1.9 (\pm 0.12) \times 10^{-2}$	93.2
17570	57133.01	4/21/15	12.5	477.01	$1.5 (\pm 0.13) \times 10^{-2}$	106.9
17571	57262.43	8/28/15	12.1	606.43	$2.8 (\pm 0.15) \times 10^{-2}$	117.9
18340	57513.25	5/5/16	29.9	857.25	$4.4 (\pm 0.12) \times 10^{-2}$	296.0
18341	57685.59	10/24/16	32.2	1029.59	$4.7 (\pm 0.12) \times 10^{-2}$	115.7
18342	57913.94	6/9/17	29.8	1257.94	$5.0 (\pm 0.13) \times 10^{-2}$	340.1
18343	58230.77	4/22/18	12.0	1574.77	$4.1 (\pm 0.18) \times 10^{-2}$	154.1
21077	58224.68	4/16/18	22.3	1568.68	$4.7 (\pm 0.15) \times 10^{-2}$	225.3
21639	58627.05	5/24/19	32.1	1971.05	$4.0 (\pm 0.11) \times 10^{-2}$	279.4
21640	58955.57	4/16/20	20.1	2300.57	$3.2 (\pm 0.13) \times 10^{-2}$	171.9
23216	58957.76	4/18/20	13.1	2301.76	$3.2 (\pm 0.16) \times 10^{-2}$	143.2

Table 3
Best-fitting Parameters from Our Spectral Analysis of Chandra X-Ray Observation of SN 2014C

Chandra ID	Phase (Days)	Γ	NH_{int} (10^{22} cm^{-2})	Flux 0.3–10 keV ($\text{erg s}^{-1} \text{ cm}^{-2}$)	Unabsorbed Flux 0.3–10 keV ($\text{erg s}^{-1} \text{ cm}^{-2}$)
16005	308	$-0.52^{+0.34}_{-0.30}$	$0.29^{+0.63}_{-0.29}$	$7.6^{+0.46}_{-2.2} \times 10^{-13}$	$7.7^{+0.46}_{-2.2} \times 10^{-13}$
17569	397	0.16 ± 0.25	$0.49^{+0.43}_{-0.41}$	$1.1^{+0.064}_{-0.18} \times 10^{-12}$	$1.1^{+0.064}_{-0.18} \times 10^{-12}$
17570	477	$-0.0063^{+0.18}_{-0.14}$	$0.057^{+0.20}_{-0.057}$	$1.2^{+0.096}_{-0.15} \times 10^{-12}$	$1.2^{+0.096}_{-0.15} \times 10^{-12}$
17571	606	0.72 ± 0.18	$0.56^{+0.23}_{-0.21}$	$9.3^{+0.69}_{-1.0} \times 10^{-13}$	$1.0^{+0.069}_{-0.1} \times 10^{-12}$
18340	857	0.83 ± 0.08	$0.40^{+0.095}_{-0.090}$	$1.2^{+0.059}_{-0.059} \times 10^{-12}$	$1.3^{+0.059}_{-0.059} \times 10^{-12}$
18341	1030	0.93 ± 0.08	$0.31^{+0.083}_{-0.079}$	$1.2^{+0.055}_{-0.056} \times 10^{-12}$	$1.3^{+0.055}_{-0.056} \times 10^{-12}$
18342	1258	1.0 ± 0.08	$0.24^{+0.078}_{-0.075}$	$1.1^{+0.049}_{-0.053} \times 10^{-12}$	$1.3^{+0.049}_{-0.053} \times 10^{-12}$
21077 and 18343	1571	$1.1^{+0.083}_{-0.082}$	$0.20^{+0.079}_{-0.076}$	$1.1^{+0.046}_{-0.053} \times 10^{-12}$	$1.2^{+0.046}_{-0.053} \times 10^{-12}$
21639	1971	$1.3^{+0.095}_{-0.093}$	$0.083^{+0.089}_{-0.083}$	$8.4^{+0.35}_{-0.44} \times 10^{-13}$	$9.2^{+0.38}_{-0.48} \times 10^{-13}$
21640 and 23216	2301	$1.3^{+0.107}_{-0.105}$	$0.15^{+0.102}_{-0.098}$	$7.2^{+0.40}_{-0.49} \times 10^{-13}$	$8.0^{+0.44}_{-0.54} \times 10^{-13}$

Table 4
NuSTAR X-Ray Observations of SN 2014C

NuSTAR ID	Date (MJD)	Date (UT)	Exposure Time (ks)	Phase (days)	Count-rate 3-79 keV (c s^{-1})	Source Significance σ
80001085002	57051.86	1/29/15	32.5	396.86	$1.4 (\pm 0.07) \times 10^{-2}$	18.9
40102014001	57122.43	4/10/15	22.4	466.43	$1.2 (\pm 0.08) \times 10^{-2}$	15.1
40102014003	57263.10	8/29/15	30.2	607.10	$1.3 (\pm 0.08) \times 10^{-2}$	17.2
40202013002	57511.78	5/3/16	43.0	856.78	$1.6 (\pm 0.07) \times 10^{-2}$	24.0
40202013004	57693.46	11/1/16	40.9	1037.46	$1.7 (\pm 0.07) \times 10^{-2}$	23.9
40302002002	57920.23	6/16/17	42.3	126.23	$1.3 (\pm 0.06) \times 10^{-2}$	21.3
40302002004	58242.67	5/4/18	40.2	1587.67	$1.4 (\pm 0.07) \times 10^{-2}$	20.9
40502001002	58635.67	6/1/19	41.5	1980.67	$9.1 (\pm 0.5) \times 10^{-3}$	16.8
40502001004	58969.80	4/30/20	54.2	2314.80	$7.8 (\pm 0.4) \times 10^{-3}$	17.5

Table 5
Joint Chandra and NuSTAR X-Ray Spectral Analysis of SN 2014C

Chandra ID	NuSTAR ID	Phase (days)	Temperature keV	$\text{NH}_{\text{int}} 10^{22} \text{cm}^{-2}$	Flux 0.3–100 keV ($\text{erg s}^{-1} \text{cm}^{-2}$)	Unabsorbed Flux 0.3–100 keV ($\text{erg s}^{-1} \text{cm}^{-2}$)
17569	80001085002	396	$18.15^{+3.6}_{-2.7}$	$2.69^{+0.34}_{-0.32}$	$1.43^{+0.17}_{-0.19} \times 10^{-12}$	$1.83^{+0.21}_{-0.24} \times 10^{-12}$
17570	40102014001	477	$23^{+7}_{-4.6}$	$1.68^{+0.23}_{-0.22}$	$1.48^{+0.24}_{-0.29} \times 10^{-12}$	$1.75^{+0.29}_{-0.34} \times 10^{-12}$
17571	40102014003	606	$22.8^{+6}_{-4.3}$	$1.30^{+0.17}_{-0.17}$	$1.58^{+0.26}_{-0.30} \times 10^{-12}$	$1.84^{+0.30}_{-0.35} \times 10^{-12}$
18340	40202013002	857	$18.86^{+2.77}_{-2.19}$	$0.942^{+0.074}_{-0.077}$	$1.79^{+0.15}_{-0.17} \times 10^{-12}$	$2.10^{+0.18}_{-0.20} \times 10^{-12}$
18341	40202013004	1029	$19.2^{+2.95}_{-2.30}$	$0.72^{+0.063}_{-0.062}$	$1.84^{+0.16}_{-0.20} \times 10^{-12}$	$2.11^{+0.18}_{-0.23} \times 10^{-12}$
18342	40302002002	1257	$17.1^{+2.38}_{-1.94}$	$0.541^{+0.057}_{-0.056}$	$1.69^{+0.16}_{-0.15} \times 10^{-12}$	$1.93^{+0.18}_{-0.17} \times 10^{-12}$
21077 and 18343	40302002004	1571	$14.9^{+1.9}_{-2.2}$	$0.469^{+0.057}_{-0.055}$	$1.50^{+0.11}_{-0.11} \times 10^{-12}$	$1.72^{+0.13}_{-0.13} \times 10^{-12}$
21639	40502001002	1971	$13.1^{+1.97}_{-1.56}$	$0.181^{+0.059}_{-0.055}$	$1.15^{+0.06}_{-0.12} \times 10^{-12}$	$1.27^{+0.07}_{-0.13} \times 10^{-12}$
21640 and 23216	40502001004	2307	$11.3^{+1.47}_{-1.19}$	$0.311^{+0.068}_{-0.066}$	$8.92^{+0.72}_{-0.72} \times 10^{-13}$	$1.03^{+0.84}_{-0.84} \times 10^{-12}$

Table 6
Properties of the Iron Emission from Combined CXO and NuSTAR

Phase (Days)	Central Energy (keV)	FWHM (keV)	Flux 6.5–7.1 keV ($\text{erg s}^{-1} \text{cm}^{-2}$)
396	$6.77^{+0.044}_{-0.043}$	$0.477^{+0.10}_{-0.10}$	$1.02^{+0.14}_{-0.13} \times 10^{-13}$
477	$6.80^{+0.048}_{-0.047}$	$0.531^{+0.11}_{-0.089}$	$1.11^{+0.16}_{-0.15} \times 10^{-13}$
606	$6.79^{+0.041}_{-0.041}$	$0.404^{+0.11}_{-0.10}$	$1.01^{+0.14}_{-0.14} \times 10^{-13}$
857	$6.72^{+0.027}_{-0.029}$	$0.241^{+0.11}_{-0.10}$	$8.33^{+1.1}_{-1.1} \times 10^{-14}$
1029	$6.73^{+0.026}_{-0.026}$	$0.461^{+0.065}_{-0.60}$	$1.41^{+0.13}_{-0.12} \times 10^{-13}$
1257	$6.75^{+0.027}_{-0.028}$	$0.364^{+0.076}_{-0.073}$	$1.01^{+0.11}_{-0.11} \times 10^{-13}$
1571	$6.71^{+0.027}_{-0.028}$	$0.332^{+0.069}_{-0.065}$	$8.99^{+1.0}_{-0.99} \times 10^{-14}$
1971	$6.73^{+0.028}_{-0.030}$	$0.298^{+0.076}_{-0.087}$	$7.07^{+0.92}_{-0.90} \times 10^{-14}$
2307	$6.69^{+0.056}_{-0.040}$	$0.467^{+0.107}_{-0.091}$	$5.26^{+0.720}_{-0.691} \times 10^{-14}$

Appendix C Example Data Table

Example tables of information for CSM properties of the interacting SNe sample contained in the supplemental

machine-readable table included in this work, shown in Tables 7 and 8.

Table 7
Mass-loss Data, Part 1

Name	Type	Group	Method	$\delta t_{\text{interact},0}$ (Days Since Explosion)	$\delta t_{\text{interact},1}$ (Days Since Explosion)	CSM Inner Radius (cm)	CSM Outer Radius (cm)
SN 1987F	IIn	3	Optical	0	unconstrained	10^{11} *	2×10^{16} *
SN 2012aa	Ic	2	Optical	65	95	5.6×10^{15}	8.2×10^{15}
iPTF13ehe	Type I SLSN	1	Optical	(128, 366)	(393, unconstrained)	4×10^{16}	$(5 \times 10^{16}, \text{unconstrained})$
SN 2014C	Ib-IIn	1	Radio, IR, Optical, X-ray	(30,130)	(1693, unconstrained)	2.2×10^{16}	10^{17}
SN 2017dio	Ic-IIn	1	Optical	(8, 18)	(83, unconstrained)	$(0.52-1.6) \times 10^{15}$	$(7.2 \times 10^{15}, \text{unconstrained})$


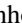





Note. *Denotes type IIn where we assume the CSM extends from 10^{11} to 2×10^{16} cm to compare the amount of CSM to that of SN 2014C.

(This table is available in its entirety in machine-readable form.)

Table 8
Mass-loss Data, Part 2

Name	Wind Velocity (km s ⁻¹)	Wind Method	\dot{M} (M_{\odot} yr ⁻¹)	M_{CSM} (M_{\odot})	$\Delta t_{\text{mass-loss}}$ (Years Prior to Explosion)	Reference
SN 1987F	150	Measured	10 ⁻²	0.42	42	Kiewe et al. (2012)
SN 2012aa	1000	Assumed	(0.58–1.2) × 10 ⁻²	(5, 10)	(1.9, 2.7)	Roy et al. (2016)
iPTF13ehe	(100, 1000)	Assumed	unconstrained	(0.01, 3)	(13, 130)	Yan et al. (2017)
SN 2014C	1000	Assumed	10 ⁻¹	(0.12, 1.2)	(7, 30)	This work
SN 2017dio	500	Measured	2 × 10 ⁻²	(8.9 × 10 ⁻² , unconstrained)	(30, 50)	Kuncarayakti et al. (2018)

ORCID iDs

Daniel Brethauer  <https://orcid.org/0000-0001-6415-0903>
 Raffaella Margutti  <https://orcid.org/0000-0003-4768-7586>
 Dan Milisavljevic  <https://orcid.org/0000-0002-0763-3885>
 Michael F. Bietenholz  <https://orcid.org/0000-0002-0592-4152>
 Ryan Chornock  <https://orcid.org/0000-0002-7706-5668>
 Deanne L. Copejans  <https://orcid.org/0000-0001-5126-6237>
 Fabio De Colle  <https://orcid.org/0000-0002-3137-4633>
 Aprajita Hajela  <https://orcid.org/0000-0003-2349-101X>
 Giacomo Terreran  <https://orcid.org/0000-0003-0794-5982>
 Felipe Vargas  <https://orcid.org/0000-0001-5518-9689>
 Lindsay DeMarchi  <https://orcid.org/0000-0003-4587-2366>
 Chelsea Harris  <https://orcid.org/0000-0002-1751-7474>
 Wynn V. Jacobson-Galán  <https://orcid.org/0000-0003-1103-3409>
 Atish Kamble  <https://orcid.org/0000-0003-0861-5168>
 Daniel Patnaude  <https://orcid.org/0000-0002-7507-8115>
 Michael C. Stroh  <https://orcid.org/0000-0002-3019-4577>

References

Anderson, G. E., Horesh, A., Mooley, K. P., et al. 2016, *MNRAS*, **466**, 3648
 Andrews, J. E., Gallagher, J. S., Clayton, G. C., et al. 2010, *ApJ*, **715**, 541
 Andrews, J. E., Krafton, K. M., Clayton, G. C., et al. 2016, *MNRAS*, **457**, 3241
 Andrews, J. E., Sand, D. J., Valenti, S., et al. 2019, *ApJ*, **885**, 43
 Andrews, J. E., & Smith, N. 2018, *MNRAS*, **477**, 74
 Arcavi, I., Gal-Yam, A., Yaron, O., et al. 2011, *ApJL*, **742**, L18
 Arcavi, I., Howell, D. A., Kasen, D., et al. 2017, *Natur*, **551**, 210
 Arnaud, K. A. 1996, in ASP Conf. Ser. 101, *Astronomical Data Analysis Software and Systems V*, ed. G. H. Jacoby & J. Barnes (San Francisco, CA: ASP), 17
 Arnett, W. D., & Meakin, C. 2011, *ApJ*, **733**, 78
 Asplund, M., Grevesse, N., Sauval, A. J., & Scott, P. 2009, *ARA&A*, **47**, 481
 Astropy Collaboration, Robitaille, T. P., Tollerud, E. J., et al. 2013, *A&A*, **558**, A33
 Balam, D. D., & Graham, M. L. 2015, *ATel*, **7931**, 1
 Balcon, C. 2020, *Transient Name Server Classification Report*, **2020-2839**
 Bauer, F. E., Dwarkadas, V. V., Brandt, W. N., et al. 2008, *ApJ*, **688**, 1210
 Ben-Ami, S., Gal-Yam, A., Mazzali, P. A., et al. 2014, *ApJ*, **785**, 37
 Ben-Ami, S., Gal-Yam, A., & Quimby, R. 2012, *CBET*, **3309**, 1
 Benetti, S. 1994, *IAUC*, **6122**, 2
 Benetti, S., Bufano, F., Vinko, J., et al. 2010, *CBET*, **2536**, 1
 Benetti, S., Chugai, N. N., Utrobin, V. P., et al. 2016, *MNRAS*, **456**, 3296
 Benetti, S., & Neuhäuser, R. 1996, *IAUC*, **6438**, 1
 Benetti, S., Zampieri, L., Pastorello, A., et al. 2018, *MNRAS*, **476**, 261
 Bhrombhakdi, K., Chornock, R., Miller, A. A., et al. 2019, *MNRAS*, **488**, 3783
 Bietenholz, M. F., Bartel, N., Argo, M., et al. 2021a, *ApJ*, **908**, 75
 Bietenholz, M. F., Bartel, N., Kamble, A., et al. 2021b, *MNRAS*, **502**, 1694

Bietenholz, M. F., De Colle, F., Granot, J., Bartel, N., & Soderberg, A. M. 2014, *MNRAS*, **440**, 821
 Bietenholz, M. F., Kamble, A., Margutti, R., Milisavljevic, D., & Soderberg, A. 2017, *MNRAS*, **475**, 1756
 Blanc, N., Bongard, S., Copin, Y., et al. 2005, *ATel*, **630**, 1
 Blondin, S., & Calkins, M. 2007, *CBET*, **1119**, 1
 Bose, S., Monard, L. A. G., Seidel, M. K., et al. 2017, *ATel*, **9937**, 1
 Bostroem, K. A., Valenti, S., Horesh, A., et al. 2019, *MNRAS*, **485**, 5120
 Bragaglia, A., Munari, U., Barbon, R., et al. 1994, *IAUC*, **6044**, 1
 Brennan, S. J., Fraser, M., Johansson, J., et al. 2022a, *MNRAS*, **513**, 5642
 Brennan, S. J., Fraser, M., Johansson, J., et al. 2022b, *MNRAS*, **513**, 5666
 Brethauer, D., Margutti, R., Milisavljevic, D., & Bietenholz, M. 2020, *RNAAS*, **4**, 235
 Bruch, R., Schulze, S., & Gal-Yam, A. 2020, *Transient Name Server Classification Report*, **2020-2170**
 Burke, J., Hiramatsu, D., Arcavi, I., et al. 2019, *Transient Name Server Classification Report*, **2019-427**
 Cartier, R., Gutierrez, C., & Yaron, O. 2017, *Transient Name Server Classification Report*, **2017-500**
 Cendes, Y., Gaensler, B. M., Ng, C.-Y., et al. 2018, *ApJ*, **867**, 65
 Cenko, S. B., Li, W., Filippenko, A. V., et al. 2012, *CBET*, **3015**, 1
 Chandra, P., Chevalier, R. A., Chugai, N., et al. 2012, *ApJ*, **755**, 110
 Chandra, P., Chevalier, R. A., Chugai, N., Milisavljevic, D., & Fransson, C. 2020, *ApJ*, **902**, 55
 Chen, T. W., Inerra, C., Fraser, M., et al. 2018, *ApJL*, **867**, L31
 Chevalier, R. A., & Fransson, C. 2006, *ApJ*, **651**, 381
 Chevalier, R. A., & Fransson, C. 2017, *Handbook of Supernovae* (Cham: Springer), 875
 Chevalier, R. A., & Liang, E. P. 1989, *ApJ*, **344**, 332
 Chomiuk, L., Chornock, R., Soderberg, A. M., et al. 2011, *ApJ*, **743**, 114
 Chornock, R., Bhrombhakdi, K., Katebi, R., et al. 2016, *ATel*, **8790**, 1
 Chugai, N., & Utrobin, V. 2022, arXiv:2205.07749
 Chugai, N. N., & Chevalier, R. A. 2006, *ApJ*, **641**, 1051
 Ciabattari, F., Mazzoni, E., Donati, S., et al. 2013, *CBET*, **3557**, 1
 Clark, P., Maguire, K., Inerra, C., et al. 2020, *MNRAS*, **492**, 2208
 Corsi, A., Kasliwal, M., Ofek, E., et al. 2012, PTF11qj: First Discovery of a Radio Luminous Ibn Supernova, *Spitzer Proposal*
 Corsi, A., Ofek, E. O., Gal-Yam, A., et al. 2014, *ApJ*, **782**, 42
 Costantin, L., Avramova-Bonche, A., Pinter, V., et al. 2018, *ATel*, **12047**, 1
 Crotts, A., Eastman, J., Depoy, D., Prieto, J. L., & Garnavich, P. 2006, *CBET*, **672**, 1
 Crowther, P. A. 2007, *ARA&A*, **45**, 177
 de Jager, C., Nieuwenhuijzen, H., & van der Hucht, K. A. 1988, *A&AS*, **72**, 259
 DeMarchi, L., Margutti, R., Dittman, J., et al. 2022, *ApJ*, **938**, 84
 Dessart, L., & John Hillier, D. 2022, *A&A*, **660**, L9
 Dewey, D., Bauer, F. E., & Dwarkadas, V. V. 2011, in AIP Conf. Ser. 1358, *GAMMA RAY BURSTS 2010*, ed. J. E. McEnery, J. L. Racusin, & N. Gehrels (Melville, NY: AIP), 289
 Dimitriadis, G., Foley, R. J., Siebert, M. R., Kilpatrick, C. D., & Corbett, H. T. 2019, *ATel*, **13375**, 1
 Dong, D. Z., Hallinan, G., Nakar, E., et al. 2021, *Sci*, **373**, 1125
 Dwarkadas, V. V., Dewey, D., & Bauer, F. 2010, *MNRAS*, **407**, 812
 Dyson, J. E. 1989, in IAU Colloq. 120, *Interstellar Wind-Blown Bubbles*, ed. G. Tenorio-Tagle, M. Moles, & J. Melnick, Vol. 350 (Berlin: Springer), 137
 Elias-Rosa, N. 2017, *Transient Name Server Classification Report*, **2017-1015**
 Filippenko, A. V. 1997, *ARA&A*, **35**, 309
 Filippenko, A. V. 1999, *IAUC*, **7220**, 1

- Filippenko, A. V., & Barth, A. J. 1997, *IAUC*, **6794**, 1
- Filippenko, A. V., & Chornock, R. 2001, *IAUC*, **7737**, 3
- Filippenko, A. V., & Foley, R. J. 2004, *IAUC*, **8452**, 3
- Filippenko, A. V., Ganeshalingam, M., Serduke, F. J. D., & Hoffman, J. L. 2004, *IAUC*, **8404**, 1
- Filippenko, A. V., & Schlegel, D. 1995, *IAUC*, **6139**, 2
- Foley, R. J., Li, W., Moore, M., et al. 2006, *CBET*, **695**, 1
- Foley, R. J., Smith, N., Ganeshalingam, M., et al. 2007, *ApJL*, **657**, L105
- Foley, R. J., Wong, D. S., Moore, M., & Filippenko, A. V. 2004, *IAUC*, **8353**, 3
- Fox, O. D., Smith, N., Ammons, S. M., et al. 2015, *MNRAS*, **454**, 4366
- Fransson, C., Ergon, M., Challis, P. J., et al. 2014, *ApJ*, **797**, 118
- Fransson, C., Lundqvist, P., & Chevalier, R. A. 1996, *ApJ*, **461**, 993
- Fraser, M., Reynolds, T., Inserra, C., & Yaron, O. 2016, *Transient Name Server Classification Report*, **2016-490**
- Fraser, M., Stritzinger, M. D., Brennan, S. J., et al. 2021, arXiv:2108.07278
- Freedman, W. L., Madore, B. F., Gibson, B. K., et al. 2001, *ApJ*, **553**, 47
- Fremling, C., & Dahiwal, A. 2019, *Transient Name Server Classification Report*, **2019-1846**
- Fremling, C., Dugas, A., & Sharma, Y. 2018, *Transient Name Server Classification Report*, **2018-1877**
- Fremling, C., Dugas, A., & Sharma, Y. 2019, *Transient Name Server Classification Report*, **2019-188**
- Fruscione, A., Silva, D. R., Doxsey, R. E., et al. 2006, *Proc. SPIE*, **6270**, 62701V
- Gagliano, A., Izzo, L., Kilpatrick, C. D., et al. 2022, *ApJ*, **924**, 55
- Gal-Yam, A. 2019, *ARA&A*, **57**, 305
- Gal-Yam, A. 2021, *Transient Name Server Classification Report*, **2021-547**
- Gal-Yam, A., Arcavi, I., Ofek, E. O., et al. 2014, *Natur*, **509**, 471
- Gal-Yam, A., Bruch, R., Schulze, S., et al. 2022, *Natur*, **601**, 201
- Gal-Yam, A., Leonard, D. C., Fox, D. B., et al. 2007, *ApJ*, **656**, 372
- Gal-Yam, A., Shemmer, O., & Dann, J. 2002, *IAUC*, **7810**, 3
- Gal-Yam, A., Yaron, O., Pastorello, A., et al. 2021, *TNSAN*, **76**, 1
- Gezari, S., Jones, D. O., Sanders, N. E., et al. 2015, *ApJ*, **804**, 28
- Gomez, S., Berger, E., Nicholl, M., et al. 2019, *ApJ*, **881**, 87
- Graessle, D. E., Silva, D. R., Doxsey, R. E., et al. 2006, *Proc. SPIE*, **6270**, 62701X
- Green, D. W. E. 2006, *IAUC*, **8689**, 3
- Green, D. W. E. 2009, *CBET*, **1780**, 2
- Groh, J. H. 2014, *A&A*, **572**, L11
- Gutiérrez, C. P., Bersten, M. C., Orellana, M., et al. 2021, *MNRAS*, **504**, 4907
- Hagen, H. J., & Reimers, D. 1997, *IAUC*, **6589**, 1
- Harris, C. E., & Nugent, P. E. 2020, *ApJ*, **894**, 122
- Haynie, A., & Piro, A. L. 2021, *ApJ*, **910**, 128
- Heathcote, S., Cowley, A., & Hartwick, D. 1988, *IAUC*, **4693**, 1
- Hiramatsu, D., Howell, D. A., Moriya, T. J., et al. 2021a, *ApJ*, **913**, 55
- Hiramatsu, D., Howell, D. A., Van Dyk, S. D., et al. 2021b, *NatAs*, **5**, 903
- Ho, A. Y. Q., Goldstein, D. A., Schulze, S., et al. 2019, *ApJ*, **887**, 169
- Holoien, T. W. S., Stanek, K. Z., Kochanek, C. S., et al. 2017, *MNRAS*, **464**, 2672
- Hosseinzadeh, G., Valenti, S., Arcavi, I., et al. 2017, *ATel*, **10059**, 1
- Howell, D. A., & Murray, D. 2012, *CBET*, **3313**, 2
- Hung, T., Dimitriadis, G., & Foley, R. J. 2019, *ATel*, **12734**, 1
- Ivanova, N., Justham, S., Chen, X., et al. 2013, *A&ARv*, **21**, 59
- Jacobson-Galán, W., Venkatraman, P., Margutti, R., et al. 2022a, *ApJ*, **932**, 58
- Jacobson-Galán, W. V., Dessart, P., Jones, D. O., et al. 2022b, *ApJ*, **924**, 15
- Jacobson-Galán, W. V., Margutti, R., Kilpatrick, C. D., et al. 2020, *ApJ*, **898**, 166
- Jin, H., Yoon, S.-C., & Blinnikov, S. 2021, *ApJ*, **910**, 68
- Jin, R., & Kong, A. K. H. 2019, *ApJ*, **879**, 112
- Kalberla, P. M. W., Burton, W. B., Hartmann, D., et al. 2005, *A&A*, **440**, 775
- Kamble, A., Margutti, R., Soderberg, A. M., et al. 2016, *ApJ*, **818**, 111
- Kiewe, M., Gal-Yam, A., Arcavi, I., et al. 2012, *ApJ*, **744**, 10
- Kilpatrick, C. D., Drout, M. R., Achettil, K., et al. 2021, *MNRAS*, **504**, 2073
- Kuncarayakti, H., Maeda, K., Ashall, C. J., et al. 2018, *ApJL*, **854**, L14
- Kundu, E., Lundqvist, P., Sorokina, E., et al. 2019, *ApJ*, **875**, 17
- Kurfürst, P., & Kr̆tička, J. 2019, *A&A*, **625**, A24
- Leung, S.-C., Fuller, J., & Nomoto, K. 2021a, *ApJ*, **915**, 80
- Leung, S.-C., Wu, S., & Fuller, J. 2021b, *ApJ*, **923**, 41
- Li, W., Wang, X., & Zhang, T. 2015, *ATel*, **6898**, 1
- Li, W. D., Li, C., Filippenko, A. V., & Moran, E. C. 1998, *IAUC*, **6829**, 1
- Liedahl, D. A., Osterheld, A. L., & Goldstein, W. H. 1995, *ApJL*, **438**, L115
- Lunnan, R., Fransson, C., Vreeswijk, P. M., et al. 2018, *NatAs*, **2**, 887
- Maeda, K., Chandra, P., Matsuoka, T., et al. 2021, *ApJ*, **918**, 34
- Margalit, B., Quataert, E., & Ho, A. Y. Q. 2022, *ApJ*, **928**, 122
- Margutti, R., Kamble, A., Milisavljevic, D., et al. 2017, *ApJ*, **835**, 140
- Margutti, R., Milisavljevic, D., Soderberg, A. M., et al. 2014, *ApJ*, **780**, 21
- Marshall, J. R., van Loon, J. T., Matsuura, M., et al. 2004, *MNRAS*, **355**, 1348
- Marston, A. P. 1997, *ApJ*, **475**, 188
- Mauerhan, J. C., Filippenko, A. V., Zheng, W., et al. 2018, *MNRAS*, **478**, 5050
- Mauerhan, J. C., Smith, N., Filippenko, A. V., et al. 2013, *MNRAS*, **430**, 1801
- Mcley, L., & Soker, N. 2014, *MNRAS*, **445**, 2492
- McNaught, R. H., Russell, K. S., James, J. M., et al. 1996, *IAUC*, **6346**, 1
- Mewe, R., Gronenschild, E. H. B. M., & van den Oord, G. H. J. 1985, *A&AS*, **62**, 197
- Mewe, R., Lemen, J. R., & van den Oord, G. H. J. 1986, *A&AS*, **65**, 511
- Milisavljevic, D., Margutti, R., Kamble, A., et al. 2015, *ApJ*, **815**, 120
- Moljaz, M., Kirshner, R., Challis, P., & Calkins, M. 2005, *CBET*, **276**, 1
- Monard, L. A. G., Milisavljevic, D., Fesen, R., et al. 2011b, *CBET*, **2946**, 1
- Monard, L. A. G., Morales Garoffolo, A., Elias-Rosa, N., et al. 2013, *CBET*, **3392**, 1
- Monard, L. A. G., Prieto, J. L., & Seth, K. 2011a, *CBET*, **2799**, 1
- Moriya, T. J. 2015, *ApJL*, **803**, L26
- Moriya, T. J., Blinnikov, S. I., Tominaga, N., et al. 2013, *MNRAS*, **428**, 1020
- Morozova, V., Piro, A. L., Fuller, J., & Van Dyk, S. D. 2020, *ApJL*, **891**, L32
- Morozova, V., Piro, A. L., & Valenti, S. 2018, *ApJ*, **858**, 15
- Nicholl, M., Blanchard, P. K., Berger, E., et al. 2020, *NatAs*, **4**, 893
- Nomoto, K., Suzuki, T., Shigeyama, T., et al. 1993, *Natur*, **364**, 507
- Ofek, E. O., Cameron, P. B., Kasliwal, M. M., et al. 2007, *ApJL*, **659**, L13
- Ofek, E. O., Sullivan, M., Cenko, S. B., et al. 2013, *Natur*, **494**, 65
- Ofek, E. O., Sullivan, M., Shaviv, N. J., et al. 2014, *ApJ*, **789**, 104
- Pastorello, A., Benetti, S., Brown, P. J., et al. 2015a, *MNRAS*, **449**, 1921
- Pastorello, A., Cappellaro, E., Inserra, C., et al. 2013, *ApJ*, **767**, 1
- Pastorello, A., Kochanek, C. S., Fraser, M., et al. 2018, *MNRAS*, **474**, 197
- Pastorello, A., Mattila, S., Zampieri, L., et al. 2008, *MNRAS*, **389**, 113
- Pastorello, A., Sauer, D., Taubenberger, S., et al. 2006, *MNRAS*, **370**, 1752
- Pastorello, A., Smartt, S. J., Mattila, S., et al. 2007, *Natur*, **447**, 829
- Pastorello, A., Wyrzykowski, L., Valenti, S., et al. 2015b, *MNRAS*, **449**, 1941
- Pastorello, A., Wang, X. F., Ciabattari, F., et al. 2016, *MNRAS*, **456**, 853
- Pellegrino, C., Howell, D. A., Terreran, G., et al. 2022, *ApJ*, **938**, 73
- Perley, D. 2021, *Transient Name Server Classification Report*, **2021-570**
- Perley, D. A., Sollerman, J., Schulze, S., et al. 2022, *ApJ*, **927**, 180
- Perley, D. A., Taggart, K., Dahiwal, A., & Fremling, C. 2020, *Transient Name Server Classification Report*, **2020-987**
- Pessi, T., Prieto, J. L., Monard, B., et al. 2022, *ApJ*, **928**, 138
- Podsiadlowski, P., Joss, P. C., & Hsu, J. J. L. 1992, *ApJ*, **391**, 246
- Pollas, C., Albanese, D., Benetti, S., Bouchet, P., & Schwarz, H. 1995, *IAUC*, **6170**, 1
- Prentice, S. J., Maguire, K., Boian, I., et al. 2020, *MNRAS*, **499**, 1450
- Prieto, J. L., Chen, P., Dong, S., et al. 2017, *RNAAS*, **1**, 28
- Prieto, J. L., McMillan, R., Bakos, G., & Grennan, D. 2011, *CBET*, **2903**, 1
- Quataert, E., & Shiode, J. 2012, *MNRAS*, **423**, L92
- Quimby, R., Castro, F., Mondol, P., Caldwell, J., & Terrazas, E. 2007, *CBET*, **793**, 1
- Quimby, R. M. 2012, in *IAU Symp. 279, Death of Massive Stars: Supernovae and Gamma-Ray Bursts*, ed. P. Roming, N. Kawai, & E. Pian (Cambridge: Cambridge Univ. Press), **22**
- Rodney, S., Trundle, C., Valenti, S., & Pastorello, A. 2009, *CBET*, **1988**, 3
- Roming, P. W. A., Pritchard, T. A., Prieto, J. L., et al. 2012, *ApJ*, **751**, 92
- Roy, R., Sollerman, J., Silverman, J. M., et al. 2016, *A&A*, **596**, A67
- Salas, P., Bauer, F. E., Stockdale, C., & Prieto, J. L. 2013, *MNRAS*, **428**, 1207
- Sana, H., de Mink, S. E., de Koter, A., et al. 2012, *Sci*, **337**, 444
- Schinzl, F. K., Taylor, G. B., Stockdale, C. J., Granot, J., & Ramirez-Ruiz, E. 2009, *ApJ*, **691**, 1380
- Schlegel, E. M. 1990, *MNRAS*, **244**, 269
- Shiode, J. H. 2013, PhD thesis, Univ. of California, Berkeley
- Shiode, J. H., & Quataert, E. 2014, *ApJ*, **780**, 96
- Shiode, J. H., Quataert, E., Cantiello, M., & Bildsten, L. 2013, *MNRAS*, **430**, 1736
- Shivvers, I., Filippenko, A. V., Silverman, J. M., et al. 2019, *MNRAS*, **482**, 1545
- Siebert, M. R., Kilpatrick, C. D., Foley, R. J., & Cartier, R. 2020, *ATel*, **13393**, 1
- Smartt, S. J. 2015, *PASA*, **32**, e016
- Smartt, S. J., Valenti, S., Fraser, M., et al. 2015, *A&A*, **579**, A40
- Smith, N. 2014, *ARA&A*, **52**, 487
- Smith, N., & Andrews, J. E. 2020, *MNRAS*, **499**, 3544
- Smith, N., Andrews, J. E., & Mauerhan, J. C. 2016, *MNRAS*, **463**, 2904
- Smith, N., & Arnett, W. D. 2014, *ApJ*, **785**, 82
- Smith, N., Chornock, R., Li, W., et al. 2008a, *ApJ*, **686**, 467
- Smith, N., Foley, R. J., Bloom, J. S., et al. 2008b, *ApJ*, **686**, 485

- Smith, N., Mauerhan, J. C., Cenko, S. B., et al. 2015, *MNRAS*, **449**, 1876
- Smith, N., & Owocki, S. P. 2006, *ApJL*, **645**, L45
- Soderberg, A. M., Chevalier, R. A., Kulkarni, S. R., & Frail, D. A. 2006, *ApJ*, **651**, 1005
- Soderberg, A. M., Gal-Yam, A., & Kulkarni, S. R. 2004, *GCN*, **2586**, 1
- Soderberg, A. M., Margutti, R., Zauderer, B. A., et al. 2012, *ApJ*, **752**, 78
- Soker, N. 2021, *ApJ*, **906**, 1
- Sollerman, J., Andersson, J., Gustafsson, M., et al. 2003, *IAUC*, **8164**, 3
- Sollerman, J., Fransson, C., Barbarino, C., et al. 2020, *A&A*, **643**, A79
- Soraisam, M., Matheson, T., Lee, C.-H., et al. 2022, *ApJL*, **926**, L11
- Stroh, M. C., Terreran, G., Coppejans, D. L., et al. 2021, *ApJL*, **923**, L24
- Strotjohann, N. L., Ofek, E. O., Gal-Yam, A., et al. 2021, *ApJ*, **907**, 99
- Sun, N.-C., Maund, J. R., & Crowther, P. A. 2020, *MNRAS*, **497**, 5118
- Suzuki, A., Nicholl, M., Moriya, T. J., & Takiwaki, T. 2021, *ApJ*, **908**, 99
- Taddia, F., Stritzinger, M. D., Fransson, C., et al. 2020, *A&A*, **638**, A92
- Taddia, F., Stritzinger, M. D., Sollerman, J., et al. 2013, *A&A*, **555**, A10
- Takáts, K., Pumo, M. L., Elias-Rosa, N., et al. 2014, *MNRAS*, **438**, 368
- Tartaglia, L. 2019, Transient Name Server Discovery Report, **2019-1671**
- Tartaglia, L., Pastorello, A., Sollerman, J., et al. 2020, *A&A*, **635**, A39
- Tartaglia, L., Sand, D. J., Groh, J. H., et al. 2021a, *ApJ*, **907**, 52
- Tartaglia, L., Sollerman, J., Barbarino, C., et al. 2021b, *A&A*, **650**, A174
- Terreran, G., Jacobson-Galan, W. V., Groh, J. H., et al. 2022, *ApJ*, **926**, 20
- Thomas, B. P., Wheeler, J. C., Dwarkadas, V. V., et al. 2022, *ApJ*, **930**, 57
- Tinyanont, S., Kasliwal, M. M., Fox, O. D., et al. 2016, *ApJ*, **833**, 231
- Tinyanont, S., Lau, R. M., Kasliwal, M. M., et al. 2019, *ApJ*, **887**, 75
- Valenti, S., Pastorello, A., Benetti, S., et al. 2011, *CBET*, **2906**, 2
- Vallely, P. J., Prieto, J. L., Stanek, K. Z., et al. 2018, *MNRAS*, **475**, 2344
- van Loon, J. T., L. Cioni, M.-R., Zijlstra, A. A., & Loup, C. 2005, *A&A*, **438**, 273
- Vargas, F., De Colle, F., Brethauer, D., Margutti, R., & Bernal, C. G. 2022, *ApJ*, **930**, 150
- Wegner, G., & Swanson, S. R. 1996, *MNRAS*, **278**, 22
- Weil, K. E., Fesen, R. A., Patnaude, D. J., & Milisavljevic, D. 2020, *ApJ*, **900**, 11
- Wellons, S., Soderberg, A. M., & Chevalier, R. A. 2012, *ApJ*, **752**, 17
- Woosley, S. E., & Heger, A. 2015, *ApJ*, **810**, 34
- Wu, S., & Fuller, J. 2021, *ApJ*, **906**, 3
- Wu, S., & Fuller, J. 2022, *ApJ*, **930**, 119
- Xiang, D., Rui, L., Wang, X., et al. 2017, *ATel*, **10376**, 1
- Yan, L., Lunnan, R., Perley, D. A., et al. 2017, *ApJ*, **848**, 6
- Yan, L., Quimby, R., Ofek, E., et al. 2015, *ApJ*, **814**, 108
- Yang, S., Sollerman, J., Chen, T.-W., et al. 2021, *A&A*, **646**, A22
- Yaron, O., Perley, D. A., Gal-Yam, A., et al. 2017, *NatPh*, **13**, 510
- Yuan, F., Quimby, R., McKay, T., et al. 2008, *CBET*, **1462**, 1